Nanoscale Advances

ROYAL SOCIETY OF CHEMISTRY

PAPER

View Article Online
View Journal | View Issue

Cite this: *Nanoscale Adv.*, 2023, **5**, 4499

Immobilized nickel boride nanoparticles on magnetic functionalized multi-walled carbon nanotubes: a new nanocomposite for the efficient one-pot synthesis of 1,4-benzodiazepines†

Farkhondeh Mohammad Aminzadeh and Behzad Zeynizadeh *

Received 14th June 2023
Accepted 22nd July 2023

DOI: 10.1039/d3na00415e

rsc.li/nanoscale-advances

In this study, a new magnetic nanocomposite consisting of Ni_2B nanoparticles anchored on magnetic functionalized multi-walled carbon nanotubes (Fe_3O_4/f-MWCNT/Ni_2B) was synthesized and characterized using various techniques such as FT-IR, XRD, FESEM, SEM-based EDX, SEM-based elemental mapping, HRTEM, DLS, SAED, XPS, BET, TGA, and VSM. The as-prepared magnetic nanocomposite was successfully employed for the preparation of bioactive 1,4-benzodiazepines from the three-component reaction of *o*-phenylenediamine (**1**), dimedone (**2**), and different aldehydes (**3**), in polyethylene glycol 400 (PEG-400) as a solvent at 60 °C. The obtained results demonstrated that the current one-pot three-component protocol offers many advantages, such as good-to-excellent yields within acceptable reaction times, favorable TONs and TOFs, eco-friendliness of the procedure, easy preparation of the nanocomposite, mild reaction conditions, a broad range of products, excellent catalytic activity, green solvent, and reusability of the nanocomposite.

1 Introduction

Benzodiazepines (BZDs) are a significant class of nitrogen-containing heterocyclic compounds known for their diverse biological properties.[1] Specifically, 1,4-benzodiazepines as a type of sedative,[2] hypnotic,[3] and myorelaxant[4] play a remarkable role in the pharmacotherapy of central nervous system (CNS) disorders.[5] Their accessibility and high efficacy contribute to their importance as a crucial scaffold in medicinal chemistry.[6] Benzodiazepines have demonstrated a wide range of pharmacological applications, some of which are mentioned here.[7] The prominent pharmacotherapeutic effects of 1,4-benzodiazepine-based medicines in the treatment of diverse CNS disorders include anti-epileptic (clobazam as an anti-epileptic, anti-convulsant, anxiolytic, and sedative drug),[8] anti-psychotic (clozapine as an anti-psychotic and anti-schizophrenia drug),[9] anti-anxiety,[10] anti-depressive,[11] anti-tumor,[12] analgesic,[13] antimicrobial,[14] anti-peptic ulcer,[15] and anticoagulant.[16] In addition, they function as inhibitors of the interleukin-1β converting enzyme (ICE),[17] hepatitis C virus (HCV) non-structural protein 5B (NS5B19), HIV-1 protease,[18] and HIV-1 non-nucleoside reverse transcriptase.[19] They also serve as cholecystokinin (CKK_2) receptor antagonists.[20] Fig. 1 illustrates a variety of extensively prescribed benzodiazepine-based medicines. Moreover, in 2023, Benoit Pelletier *et al.* found benzodiazepine-based inhibitors of the E2 enzyme UBCH10, which have a significant function in the degradation of the protein p21. The inhibitors were discovered through a cell-based screening procedure for compounds that could inhibit the degradation of p21. The implications of this discovery could be significant, especially in the realm of cancer treatment.[21] In another research study, Seegehalli Anil *et al.* reported the potential of benzodiazepines to inhibit the growth of *Mycobacterium tuberculosis* (*M. tb*) as a promising treatment option for anti-tuberculosis.[22] Additionally, Paolo Fruscella *et al.* conducted a study on the anti-inflammatory properties of 1,4-benzodiazepine tricyclic derivatives. Their research revealed that these derivatives have the ability to inhibit interleukin-6 and prostaglandin E(2), making them a promising treatment option for inflammation.[23] In 2019, Mehrazar *et al.* investigated the design and synthesis of benzodiazepine-1,2,3-triazole hybrids, a novel class of molecules that demonstrate high inhibitory activity against the butyrylcholinesterase enzyme. The mentioned enzyme is a significant target for drug development due to its involvement in the pathogenesis of Alzheimer's disease.[24] Ursini *et al.* focused on the design and synthesis of new 1-[(3*R*)-1-(1-adamantylmethyl)-2,4-dioxo-5-phenyl-1,5-benzodiazepin-3-yl]-3-phenylurea (GV150013) as a potential cholecystokinin-B (CCKB) receptor antagonist.[25] These studies demonstrate promising potential for advancing research and development in the synthesis of 1,4-

Department of Chemistry, Urmia University, Urmia 5756151818, Iran. E-mail: aminzadeh67@gmail.com; bzeynizadeh@gmail.com

† Electronic supplementary information (ESI) available. See DOI: https://doi.org/10.1039/d3na00415e

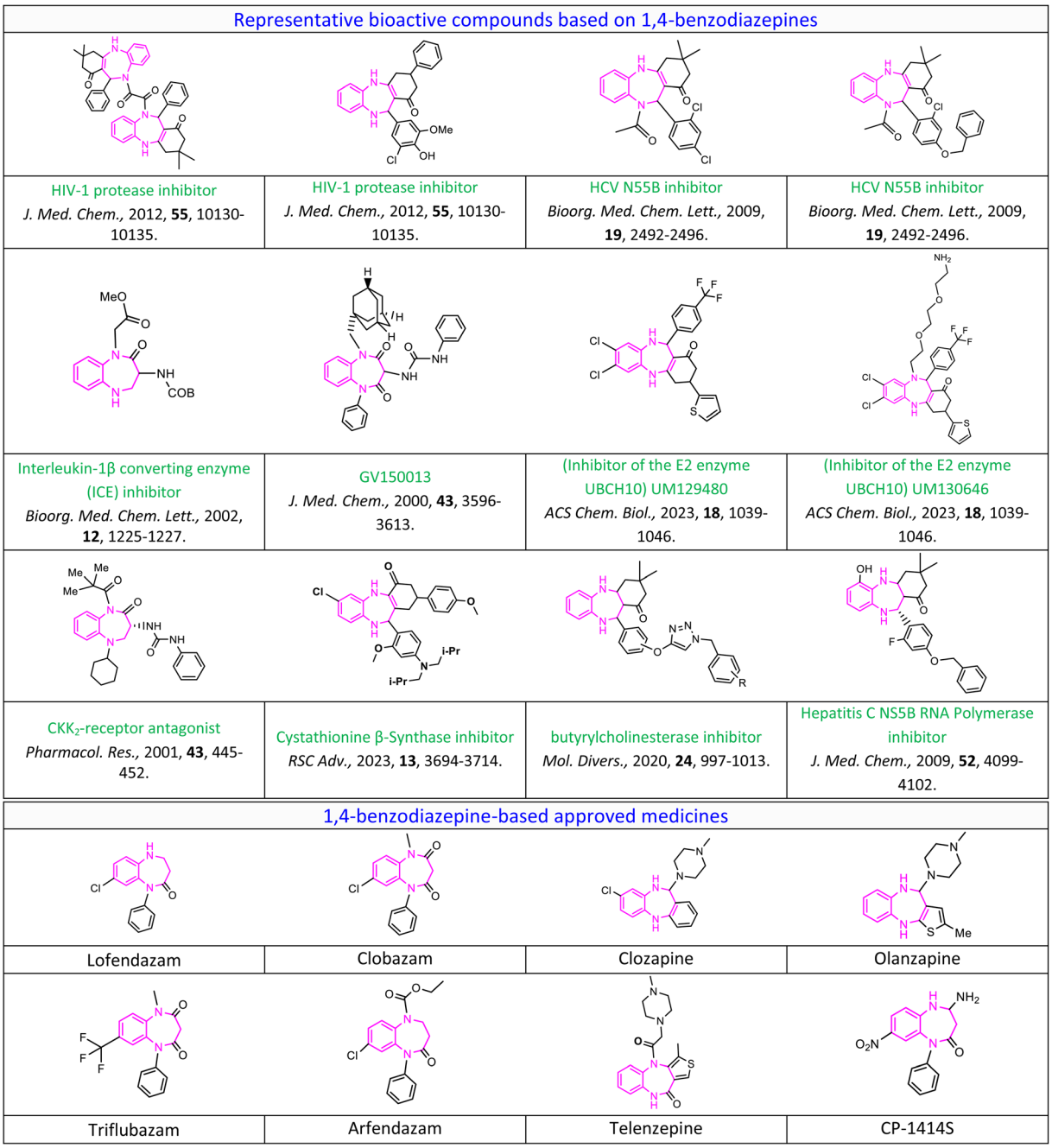

Fig. 1 1,4-Benzodiazepine-based biological active compounds.

benzodiazepines in medicinal chemistry. This highlights an opportunity for further research, exploration, and study in this domain.

Nowadays, researchers have increasingly turned to green chemistry protocols (GCPs), which is a leading approach for designing and synthesizing pharmaceuticals.[26] This popular choice is driven by its environmentally sustainable advantages. Among researchers, there is a targeted effort to develop novel, effective, and medicinally active compounds based on the 1,4-benzodiazepines scaffold employing meticulous and systematic synthetic strategies rooted in green chemistry principles. Implementation of more sustainable green chemistry principles in the pharmaceutical industry demands a significant effort to shift from conventional methods to newer, eco-friendly approaches.[27] In this regard, one of the most attractive and widely explored green synthetic approaches in the field of organic synthesis and medicinal chemistry is the focus on one-pot synthesis, specifically through multicomponent reactions (MCRs).[28] MCRs are one-pot reactions in which at least three reactants join through the formation of covalent bonds to give highly selective products.[29] By simple reaction design, low energy consumption, streamlined work-up procedures, and containing all or most of the atoms of the starting materials, MCRs greatly improve step- and atom-economy and reduce

waste, making them an ideal option for green and environmentally conscious processes.[30] These characteristics significantly enhance MCRs as prominent and active procedures in the domains of drug discovery and pharmaceutical synthesis, establishing their indispensability in the field.[31] Overall, the advantages of MCRs make them a crucial approach for contemporary chemists to fulfill the requirements of sustainable green chemistry effectively.[32]

In order to achieve optimal results during the synthesis process, the accurate selection of reaction solvent and catalyst based on GCPs, along with the accurate selection of reaction method is crucial. In recent years, extensive investigations have been devoted to exploring the applicability of one-pot multicomponent reactions (MCRs) in the development of facile, straightforward, and highly efficient methodologies for the synthesis of a broad range of 1,4-benzodiazepines.[18] Among them, a number of catalytic systems and methodologies for the synthesis of 1,4-benzodiazepines based on the condensation of *o*-phenylenediamine with dimedone and various aldehydes, each of which holds a unique position in the synthesis of heterocyclic compounds, have been reported by researchers, such as UiO-66 MOF,[31] $La_2O_3/La(OH)_3$,[33] GO nanosheets,[34] Gr@TiO_2 NCs,[35] Cu(II)/PI-COF,[36] acetic acid/water under microwave irradiation,[37] sulfated polyborate,[38] $B(HSO_4)_3$,[39] L-proline,[40] $CuFe_2O_4$,[41] $Fe(OTs)_3/SiO_2$,[42] $CoFe_2O_4$@GO-K22,[43] $CoFe_2O_4$@SiO_2@NH-NH_2-PCuW,[44] CeO_2/CuO@GQDs@NH_2,[45] [H-PFBA][PF_6],[46] [H-NMP][HSO_4],[47] ZnS nanoparticles,[48] Fe_3O_4@-chitosan,[49] Fe(III)-NicTC@nSiO_2,[50] $SrFe_{12}O_{19}$,[51] chitosan functionalized by triacid imide,[52] HBF_4–SiO_2,[53] SPINOL-derived chiral phosphoric acid,[54] and oxalic acid.[55] Although each of these methods has its own advantages, they also have several shortcomings that need to be addressed. These include prolonged reaction times, effortful workup, difficulties with catalyst recovery and reusability, and reliance on toxic reagents that can be problematic. Therefore, it is highly crucial to develop rapid, clean, efficient, and eco-friendly reaction procedures as well as utilize cost-effective and recyclable catalysts to improve sustainability.

As a part of our ongoing commitment to advancing one-pot organic synthesis reactions, we have investigated the efficacy of immobilized nickel boride on magnetic multi-walled carbon nanotubes as a new nanocomposite for the synthesis of 1,4-benzodiazepines. This innovative approach demonstrates promising potential for improving the efficiency of benzodiazepines synthesis. This trend is motivated by the objectives of easy preparation, reusability, and environmental sustainability.

In recent years, numerous literature sources have highlighted the diverse and remarkable applications of functionalized multi-walled carbon nanotubes, emphasizing their significant material properties, especially in catalysis. This has resulted in high demand for these multipurpose innovative nanostructures.[56] These reports underscore the considerable value of these carbon scaffolds. Their unique hollow structure and extensive surface area make them highly porous,[57] as well as their first-rate thermal stability, electrical conductivity due to the large π-conjugated system and strong C=C bonds, and excellent mechanical damage resistance, make them a top choice for a widespread range of applications.[58] Notably, they also have a remarkable affinity for interacting with organic materials, further expanding their potential use.[59] However, their properties can be further improved or customized to meet specific application requirements by chemical modification.[60] This involves integrating relevant functional groups and or nanoparticles into the MWCNTs to attain desired structures or attach suitable nano-objects.[61] In fact, research has shown that modifying multi-walled carbon nanotubes with compounds of different chemical nature can significantly enhance their dispersity in solvents, further increasing their application potential.[62] In the literature, chemical functionalization of MWCNTs for modification of their surface by the incorporation of –COOH on the exterior surfaces to achieve different objectives such as drug delivery, cancer therapy, diagnostics, and electronic devices has been widely conducted.[63] According to scientific knowledge, –COOH functional groups and defects on multi-walled carbon nanotubes act as active sites that facilitate specific catalytic reactions.[64]

In catalytic applications, MWCNTs present a challenge in terms of separation from reaction mixtures due to their naturally diamagnetic characteristics.[65] However, one effective solution to overcome this drawback is to induce magnetism into MWCNTs. They can be functionalized with Fe_3O_4 magnetic nanoparticles, a mixed valence (Fe^{II}–Fe^{III}) n-type semiconductor, having various practical applications.[66] By implementing this strategy, catalysis systems become highly active, dispersible, and can be recovered using an external magnet. In addition, the mechanical, electrical, and thermo-optical properties of MWCNTs can be further enhanced by interacting with Fe_3O_4. This complex combination results in a superparamagnetic behavior, yielding a high-strength magnetic material that can be utilized in various fields.[67] This not only conserves energy and the environment but also leads to the production of target products at a low cost and under mild and green conditions. In the contemporary scientific landscape, the surface properties of multi-walled carbon nanotubes have been the subject of intense research as researchers seek to optimize their performance for various applications. Magnetic MWCNTs can afford an opportunity to achieve a new catalyst with high performance due to operational simplicity, easy separation, low cost, high efficiency, effective recovery, and reusability.[68] Further, the integration of magnetic compounds with highly active transition metal-rich borides (TMBs) results in the assembly of different properties, which leads to synergistic activities, including increased catalytic capability and enhancement of stability or conductivity, and also prevents Fe_3O_4 aggregation.[69] The inclusion of boron into transition metals can bring about notable modifications in metal-active centers. This is attributed to the unique metalloid nature of boron, which exhibits smaller electronegativity and atomic radius compared to transition metals.[70] Among them, nano nickel boride has been extensively studied due to its effectiveness in catalysis,[71] high microhardness,[72] excellent selectivity and activity for liquid phase reaction,[73] high chemical and thermal stability,[74] and potential applicability in biochemistry.[75]

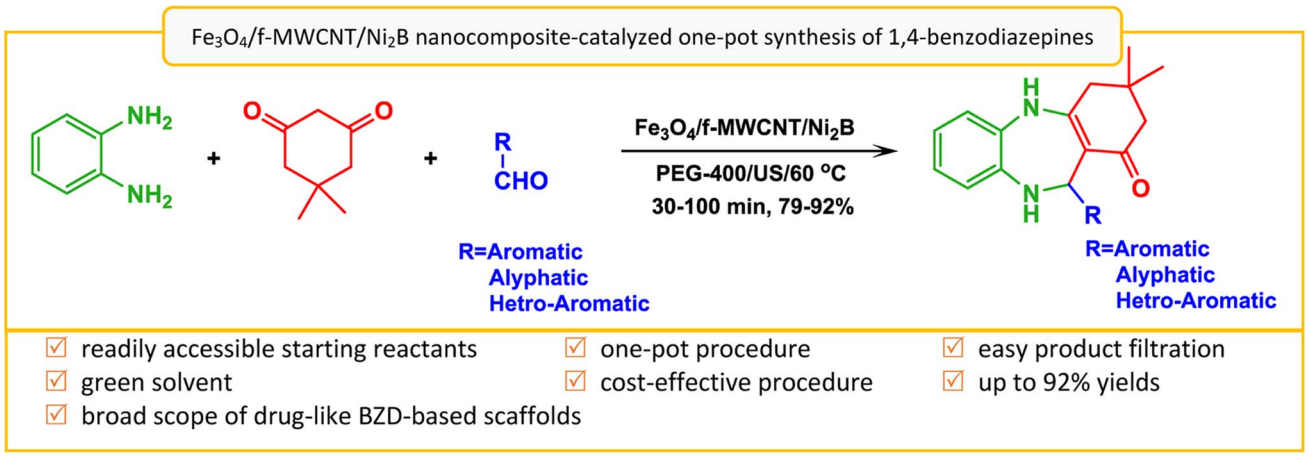

Scheme 1 Fe_3O_4/f-MWCNT/Ni_2B nanocomposite-catalyzed one-pot three-component synthesis of 1,4-benzodiazepines.

This integration of diverse materials engenders a pioneering approach to developing the production of functional materials.

In light of the aforementioned findings and in our continued interest in designing new catalytic platforms[76] and preparing multi-walled carbon nanotube-based materials,[77] we aim to present a convenient strategy for the preparation of a new Ni_2B-decorated magnetic multi-walled carbon nanotubes support (Fe_3O_4/f-MWCNT/Ni_2B) as an efficient nanocomposite. We also investigate its catalytic activity for the one-pot three-component synthesis of 3,3-dimethyl-11-alkyl/aryl/hetroaryl-2,3,4,5,10,11-hexahydro-1*H*-dibenzo[*b*,*e*][1,4]diazepin-1-ones from *o*-phenylenediamine (**1**), dimedone (**2**), and various aliphatic/aromatic/heteroaromatic aldehydes (**3a–o**) in polyethylene glycol (PEG-400) as solvent (Scheme 1). By using this nanocomposite, a large number of derivatives were prepared with good-to-excellent yields and acceptable reaction times. Furthermore, the as-prepared nanocomposite has several advantages such as easy work-up procedures, and recyclability of the nanocatalyst.

2 Experimental

2.1 Materials and reagents

The carboxylic acid functionalized multi-walled carbon nanotubes (MWCNTs-COOH) were procured from Nanocyl, Belgium, with a purity of >95%, –COOH content of 0.73 wt%, a length of 0.5–500 μm, and an outer diameter of 10–50 nm. Ferrous chloride tetrahydrate ($FeCl_2 \cdot 4H_2O$), ferric chloride hexahydrate ($FeCl_3 \cdot 6H_2O$), ammonium hydroxide (NH_4OH, 25%), $Ni(OAc)_2 \cdot 4H_2O$, ethanol, ethylene glycol (EG), sodium borohydride ($NaBH_4$), polyethylene glycol 400 (PEG-400), benzaldehydes, dimedone, and *o*-phenylenediamine were purchased from Merck and Sigma-Aldrich companies and utilized without further processing or purification.

2.2 Characterization

Ultrasonic irradiation was carried out using a SOLTEC SONICA 2400MH S3 (300 W). The FT-IR spectrum was recorded using the KBr pellet method with an IR spectrometer (Thermo Nicolet Nexus 670 spectrometer) in the range 4000–400 cm^{-1}. ^1H NMR spectra were recorded using a Bruker Avance 300 and 400 MHz spectrometer. The XRD analysis was performed using powder X-ray diffraction (PXRD) using a Philips PANalytical X'PertPro diffractometer (The Netherlands) in 40 kV and 30 mA with Cu-Kα radiation ($\lambda = 1.5406$ Å). The SEM images, EDX diagram, and elemental mapping were obtained from an FESEM-TESCAN MIR A3 scanning microscope. The high-resolution transmission electron microscopy (HR-TEM) images were obtained using a HR-TEM FEI TECNAI F20 (200 kV) transmission electron microscope. XPS analysis was done in the count rates (c per s) between 0 and 1200 eV using a surface science instrument BESTEC (EA 10) with a monochromatic Mg Kα X-ray source ($h\nu = 1253.6$ eV) to see the changes or impurities that may occur in the structure. The total pore volume, specific surface area, and distribution of the pore size of nanocomposites were measured by the Barrett–Brunauer–Emmett–Teller (BET) and Joyner–Halenda (BJH) methods using a Belsorp-Max, Japan, respectively. Thermogravimetric analysis (TGA/DTA) of the synthesized nanocomposites was done in the temperature range of 0–800 °C and the heating rate was 10 °C per min using the SDT Q600 instrument from TA instruments. The magnetic properties of the nanocomposites were measured using a lakeshore (Model 7410) vibrating sample magnetometer (VSM) at room temperature under magnetic fields up to 20 kOe. Purity assessment and reaction monitoring of the products were performed using thin-layer chromatography (TLC) over a silica gel 60 F254 aluminum sheet.

2.3 Synthetic methods

2.3.1 Synthesis of magnetic f-MWCNT (Fe_3O_4/f-MWCNT).[77]

Fe_3O_4/f-MWCNT nanocomposites were synthesized by a co-precipitation method of Fe^{2+} and Fe^{3+} with a molar ratio of 1 : 2 in an alkaline solution in the presence of MWCNT-COOH. Primarily, in a three-necked round-bottom flask (250 mL), 0.5 g of MWCNT-COOH was dispersed in 100 mL deionized water by ultrasonication for 30 min. Then, 0.6 g of $FeCl_3 \cdot 6H_2O$ and 0.32 g of $FeCl_2 \cdot 4H_2O$ were added to the above solution

under ultrasonication for another 30 min. Next, 40 mL of NH_4OH (25%) was added dropwise to the reaction mixture under a nitrogen atmosphere and the mixture was stirred for 2 h at 60 °C. Upon completion of the reaction and cooling to room temperature, 3 mL of ethanol was added to the reaction mixture and stirred for 2 min. Ultimately, the obtained precipitate was magnetically extracted, washed using deionized water, and subjected to drying at 50 °C.

2.3.2 Synthesis of Fe_3O_4/f-MWCNT/Ni_2B nanocomposites. In brief, 1 g of Fe_3O_4/MWCNT was dispersed in 20 mL of deionized water by ultrasonication for 10 min. Then, dissolved $Ni(OAc)_2 \cdot 4H_2O$ (1.244 g, 5 mmol in 50 mL of distilled water) was added to the solution under ultrasonication for 10 min. After that, under a nitrogen atmosphere, $NaBH_4$ (10 mL, 1 M) was added in a dropwise manner to the above reaction medium at room temperature. Upon addition of $NaBH_4$ solution to the reaction mixture, a black precipitate was concomitantly obtained with the release of hydrogen gas. After the hydrogen gas had been completely released from the reaction medium, a further 5 mL of 1 M $NaBH_4$ solution was re-dropped into the reaction mixture under an air atmosphere and stirred for 15 min. After the reaction was completed, 3 mL of ethanol was added to the reaction mixture and stirred for 2 min. Ultimately, the obtained precipitate was magnetically extracted, washed using deionized water, and subjected to drying at 50 °C.

2.3.3 General procedure for synthesis of 1,4-benzodiazepines catalyzed by the as-synthesised Fe_3O_4/f-MWCNT/Ni_2B nanocomposite. A mixture of *o*-phenylenediamine (1 mmol), dimedone (1 mmol), and Fe_3O_4/f-MWCNT/Ni_2B (10 mg) in 3 mL polyethylene glycol 400 in a round bottom flask (50 mL) was ultrasonicated at 60 °C for 15 min. When the preparation of the intermediate was confirmed using TLC, an aliphatic/aromatic/heteroaromatic aldehyde (1 mmol) was added, and the reaction was continued for the appropriate time at 60 °C. At the end of the reaction, as indicated by TLC, the reaction mixture was cooled to room temperature, and the nanocatalyst was separated using an external magnetic field. As the next step, the reaction mixture was washed with water (3 × 20 mL) to remove polyethylene glycol 400 and then filtered, followed by recrystallization in hot ethanol to afford pure 1,4-benzodiazepines. Afterward, the extracted catalyst was washed several times with water and ethanol and dried in a vacuum at 50 °C for the next run to investigate recyclability.

3 Results and discussion

3.1 Synthesis of the Fe_3O_4/f-MWCNT/Ni_2B nanocomposite

In continuation of our interest in the synthesis of heterocyclic compounds using MCRs in the presence of noncatalytic systems,[77] herein, an active, efficient, and magnetic nanocomposite system for the synthesis of benzodiazepine derivatives *via* a one-pot three-component condensation reaction of *o*-phenylenediamine (**1**), dimedone (**2**), and various aliphatic/aromatic/heteroaromatic aldehydes (**3a–o**) is introduced. In

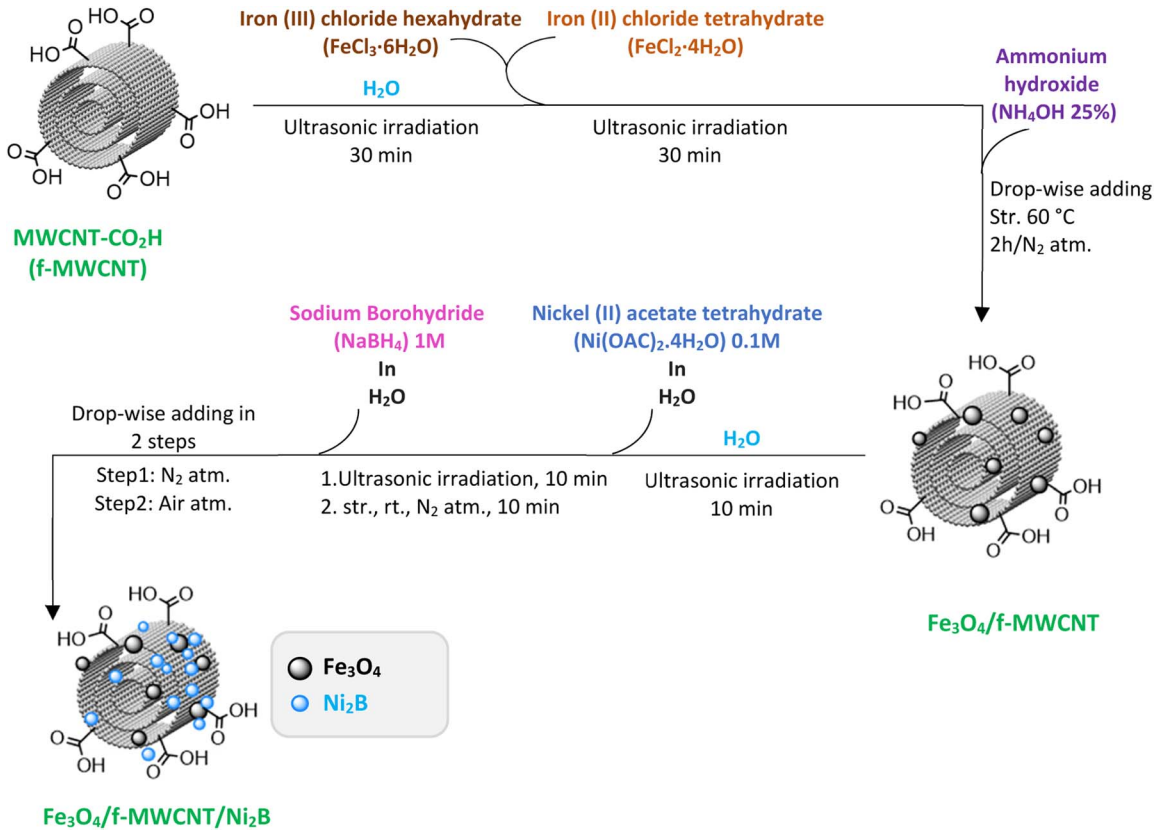

Scheme 2 Schematic illustration of the preparation of the Fe_3O_4/f-MWCNT/Ni_2B nanocomposite.

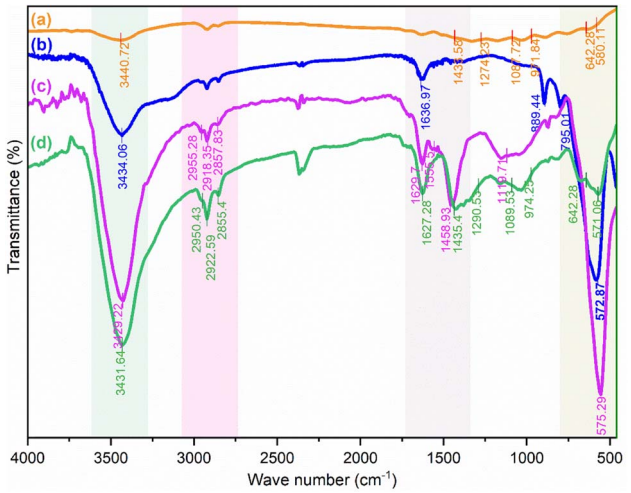

Fig. 2 FT-IR spectra of (a) Ni_2B, (b) Fe_3O_4, (c) Fe_3O_4/f-MWCNT, and (d) Fe_3O_4/f-MWCNT/Ni_2B nanocomposites.

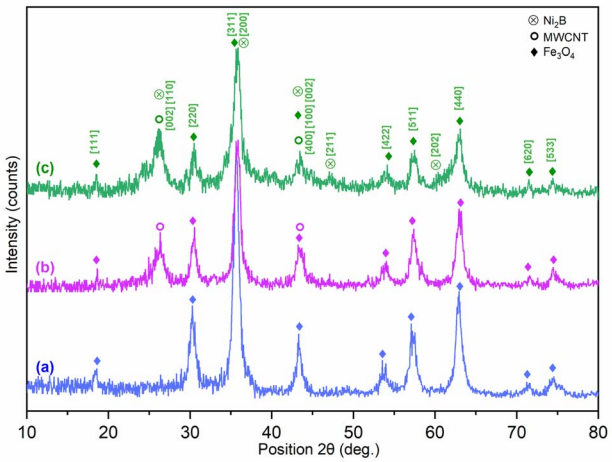

Fig. 3 XRD pattern of (a) Fe_3O_4, (b) Fe_3O_4/f-MWCNT, and (c) Fe_3O_4/f-MWCNT/Ni_2B nanocomposites.

this regard, to prepare this new nanocomposite system, first the pristine carboxylic acid functionalized multi-walled carbon nanotubes (f-MWCNTs) were magnetized through the chemical co-precipitation of Fe^{2+} and Fe^{3+} in an alkaline solution. In the next step, the procedure for immobilization of nickel boride (Ni_2B) by $Ni(OAc)_2 \cdot 4H_2O$ as a source of Ni through the dropwise addition of $NaBH_4$ as both boron source and a reducing agent was executed on the magnetic functionalized multi-walled carbon nanotube (Fe_3O_4/f-MWCNT) matrix. It's noteworthy that borides are oxidizable in the presence of air. As a result, for the modification reaction of the magnetic functionalized multi-walled carbon nanotubes (Fe_3O_4/f-MWCNT) with Ni_2B, a nitrogen atmosphere is required. The sequential progression of each step is outlined in detail (Scheme 2). The successful preparation of the Fe_3O_4/f-MWCNT/Ni_2B nanocomposite is confirmed by FT-IR, XRD, FESEM, SEM-based EDX, SEM-based elemental mapping, HRTEM, DLS, SAED, XPS, BET, TGA, and VSM.

3.2 Characterization of the Fe_3O_4/f-MWCNT/Ni_2B nanocomposite

3.2.1 FT-IR analysis. Fourier-transform infrared spectroscopy (FT-IR) was employed for confirmation of the existence of functional groups in the synthesized nanocomposite system using the potassium bromide (KBr) disk method in the region 400–4000 cm^{-1}. Fig. 2 shows the FT-IR spectra of Fe_3O_4, Fe_3O_4/f-MWCNT, Ni_2B, and Fe_3O_4/f-MWCNT/Ni_2B nano-materials. In the FT-IR spectrum of bare Fe_3O_4 nanoparticles (Fig. 2b), the absorption bands around 582, 1636, and 3433 cm^{-1} are corresponding to the stretching vibrations of Fe–O, bending and stretching vibrations of hydroxyl groups (–OH) and adsorbed water molecules, respectively.[76] For Fe_3O_4/f-MWCNT (Fig. 2c), the absorption peaks at 1120, 1555, 1629, and 3429 cm^{-1} are attributed to the stretching vibration of C–O, C=C, C=O, and –OH of the carboxylic acid group (–CO_2H), respectively. In addition, the weak peaks around 2922 and 2950 cm^{-1} can be attributed to asymmetric and symmetric CH_2 stretching. In addition, the Fe_3O_4/f-MWCNT nanocomposite shows a new band at 575 cm^{-1} which can be related to the Fe–O stretching vibrations.[78] This peak confirms the formation of Fe_3O_4 nanoparticles on MWCNT-COOH. Furthermore, the FTIR spectrum of the Fe_3O_4/f-MWCNT/Ni_2B (Fig. 2d), in addition to the aforementioned peaks, illustrates peaks related to the presence of Ni_2B (Fig. 2a). These include a peak at 642 cm^{-1} corresponding to the bending vibrations of BO_4 and a peak at 1089 cm^{-1} related to BO_2 symmetrical stretching vibrations, as well as peaks at 974, 1290, and 1435^{-1} that can be attributed to both symmetric and asymmetric stretching vibrations of B_2O_3 or BO_3.[71j,k,79] All of these data support the manifestation that the Fe_3O_4/f-MWCNT is successfully modified by Ni_2B. Therefore, these results clearly confirm the successful synthesis of the Fe_3O_4/f-MWCNT/Ni_2B nanocatalyst.

3.2.2 XRD analysis. The powder X-ray diffraction (PXRD) spectra are recorded in the range of Bragg angles ($2\theta = 10°$–$80°$)

Table 1 XRD data of as-synthesized Fe_3O_4/f-MWCNT/Ni_2B nanocomposites

No.	Pos. [2Th]	*d*-spacing [A]	Phase	[*hkl*]
1	18.4877	4.19016	Fe_3O_4	[111]
2	26.2734	3.39209	MWCNT	[002]
			Ni_2B	[110]
3	30.4956	2.93139	Fe_3O_4	[220]
4	35.8109	2.50754	Fe_3O_4	[311]
			Ni_2B	[200]
5	43.3896	2.08552	Fe_3O_4	[400]
			Ni_2B	[002]
			MWCNT	[100]
6	47.2015	1.92401	Ni_2B	[211]
7	53.9317	1.70012	Fe_3O_4	[422]
8	57.5399	1.6018	Fe_3O_4	[511]
9	60.4985	1.52903	Ni_2B	[202]
10	62.9884	1.47573	Fe_3O_4	[440]
11	71.6453	1.31612	Fe_3O_4	[620]
12	74.9333	1.26632	Fe_3O_4	[533]

at room temperature to investigate the crystallinity character and phase purity of Fe_3O_4, Fe_3O_4/f-MWCNT, and Fe_3O_4/f-MWCNT/Ni_2B nanocomposite systems (Fig. 3 and Table 1). As can be seen in Fig. 3a, the diffraction peaks at $2\theta = 18.49°$ (111), 30.49° (220), 35.81° (311), 43.38° (400), 53.93° (422), 57.54° (511), 62.99° (440), 71.64° (620), and 74.93° (553) for bare Fe_3O_4 nanoparticles are in agreement with the standard one of Fe_3O_4 (JCPDS No. 01-075-0449, 00-008-415, 79-0418, and 74-2402).[80] These are attributed to the inverse cubic spinel structure of magnetic nanoparticles with the *Fd3m* symmetry group, confirming the high purity and crystallinity character of the magnetite sample. Also, the lattice parameter of the magnetite Fe_3O_4 was estimated to be 8.3100 angstroms. The XRD pattern of Fe_3O_4/f-MWCNT (Fig. 3b) also shows a broad peak at $2\theta =$ 43.39° (100) that overlapped with the peak of Fe_3O_4 and $2\theta =$ 26.27° representing the lattice reflection plane (002) corresponding to the graphite structure of f-MWCNTs (JCPDS card no. 00-008-0415 and 75-1621).[81] In this spectrum, the presence of similar peaks of Fe_3O_4 in the Fe_3O_4/f-MWCNT nanocomposite system confirms the successful grafting of Fe_3O_4 to MWCNT-COOH. For the Fe_3O_4/f-MWCNT/Ni_2B nanocomposite (Fig. 3c), the adaption of additional peaks to reference patterns has proven that the detected peaks are consistent with the tetragonal crystal structure of Ni_2B (nickel boride), with the *I*4/*mcm* symmetry group. As can be observed, the diffraction pattern shows peaks at 47.20° and 60.49° for diffraction planes with Miller index (211) and (202), respectively. Furthermore, the peaks at 26.27° (110), 35.81° (200), and 43.39° (002) that

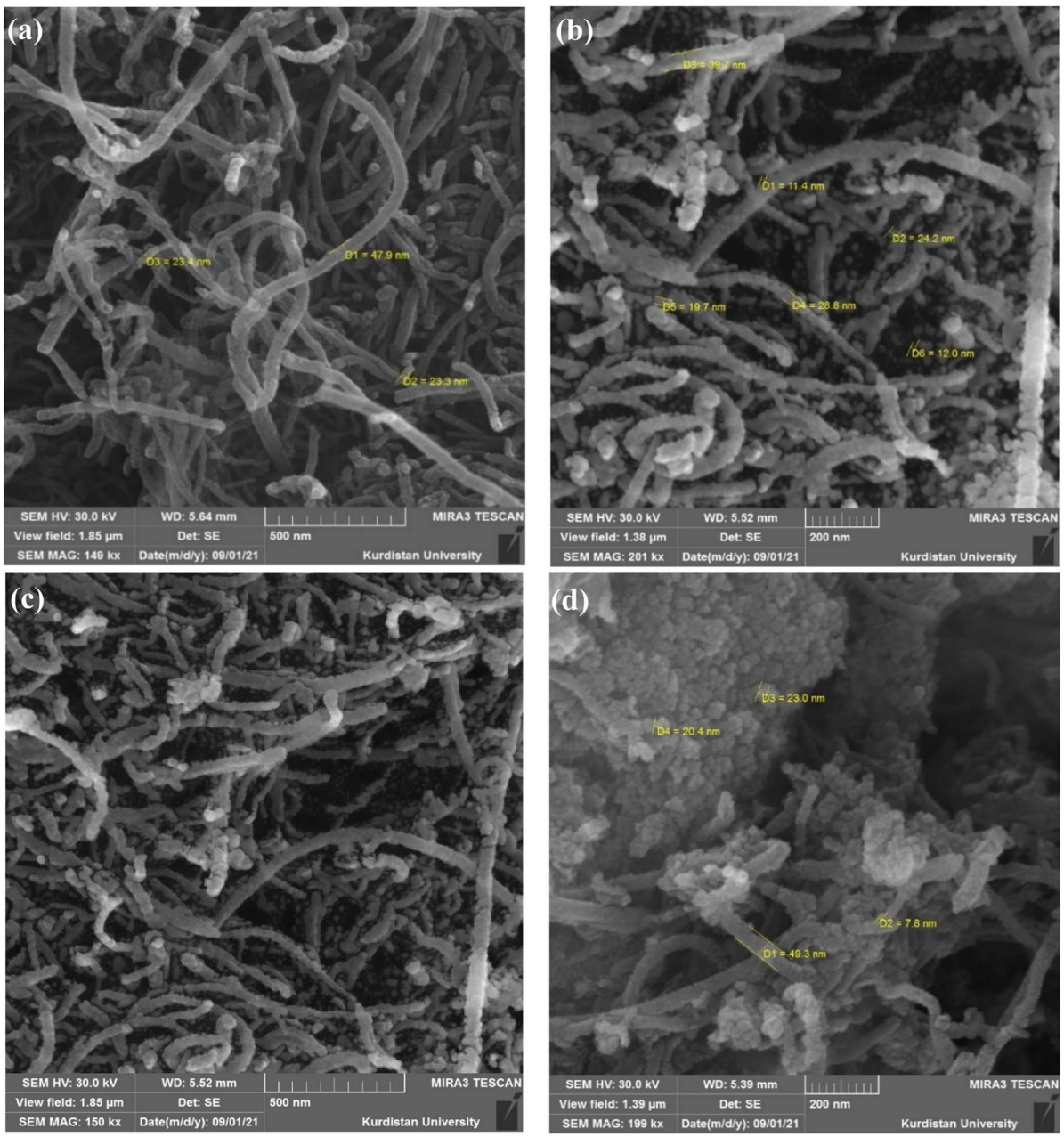

Fig. 4 FESEM images of (a) MWCNT-COOH, (b and c) Fe_3O_4/f-MWCNT, (d) Fe_3O_4/f-MWCNT/Ni_2B nanocomposites.

correspond to nickel boride were found to overlap with similar peaks in Fe_3O_4/f-MWCNT (JCPDS No. 00-048-1222). The aforementioned observations provide confirmation of the successful formation of the desired nanocomposite system. The X-ray diffraction analysis can provide information about the crystallite size as one of its discernible outcomes. By applying the Debye–Scherrer equation ($D = K\lambda/\beta \cos\theta$), the crystallite sizes of the Ni_2B and Fe_3O_4 phases in the synthesized nanocomposite were found to be 9.5 and 8.4 nm, respectively. However, the non-spherical morphology of the carbon nanotube phase makes it unsuitable to estimate its crystal size using the Debye–Scherrer equation.

3.2.3 FESEM analysis. The structural morphology of the as-synthesized Fe_3O_4/f-MWCNT/Ni_2B nanocomposite was investigated using field emission scanning electron microscopy (FESEM). Fig. 4 shows the FESEM images of MWCNT-COOH, Fe_3O_4/f-MWCNT, and Fe_3O_4/f-MWCNT/Ni_2B nanocomposites. It is clear from Fig. 4a that the pristine MWCNT-COOH consists of highly tangled tubes with an average diameter of approximately 24 nm. Analysis of FESEM images of Fe_3O_4/f-MWCNT (Fig. 4b and c) indicates the presence of iron, which is observed as bright points due to its high capacity for electron backscattering, resulting in a brighter appearance. It clearly shows that nanoparticles of Fe_3O_4 are uniformly distributed on

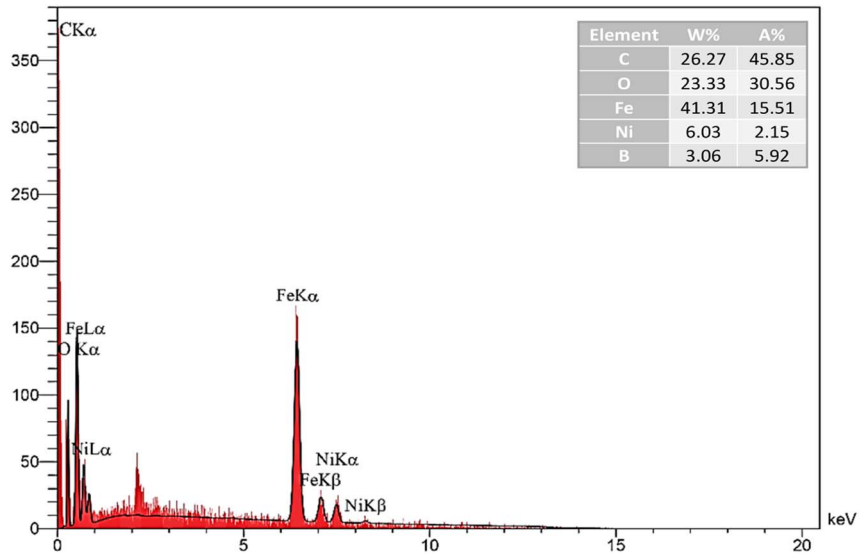

Element	W%	A%
C	26.27	45.85
O	23.33	30.56
Fe	41.31	15.51
Ni	6.03	2.15
B	3.06	5.92

Fig. 5 SEM-based EDX diagram of the as-synthesized Fe_3O_4/f-MWCNT/Ni_2B nanocomposite.

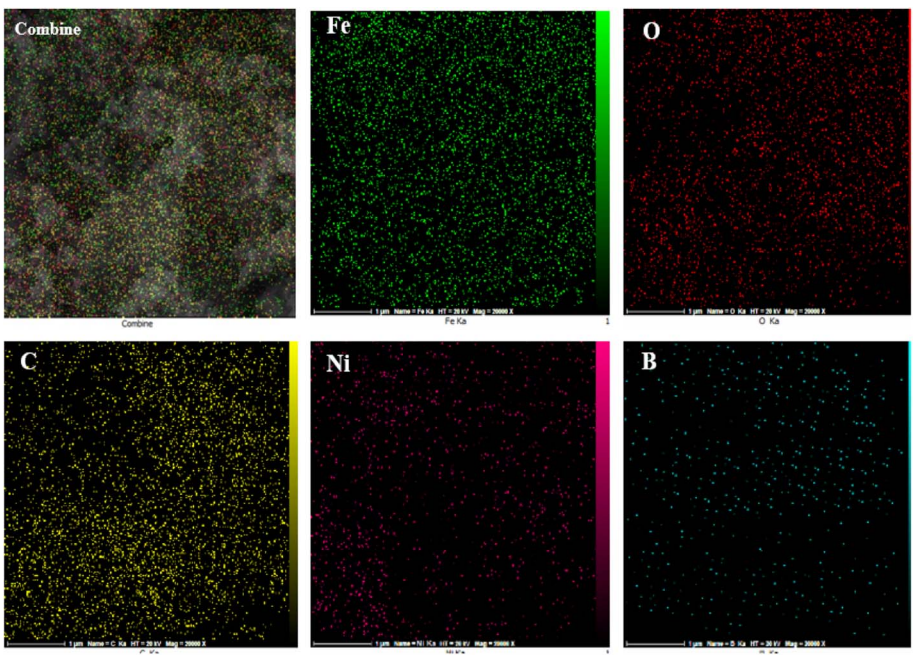

Fig. 6 SEM-based elemental mapping of the as-synthesized Fe_3O_4/f-MWCNT/Ni_2B nanocomposite.

the surface of MWCNT-COOH which confirms that magnetic nanoparticles successfully attached to the surface of the MWCNT-COOH. By comparing the FESEM images of Fe_3O_4/f-MWCNT/Ni_2B and Fe_3O_4/f-MWCNT, it can be concluded that the large lumps on the surface of Fe_3O_4/f-MWCNT are related to the attached Ni_2B nanoparticles (Fig. 4d). Meanwhile, the rougher structures of Fe_3O_4/f-MWCNT/Ni_2B could be attributed to the successful surface coating from Fe_3O_4/f-MWCNT with Ni_2B nanoparticles. Generally, the obtained results highlighted that the Fe_3O_4 and Ni_2B nanoparticles are well stabilized without changing the main structure of MWCNT-COOH.

3.2.4 SEM-based EDX and SEM-based mapping analysis. The elemental composition of the as-synthesized Fe_3O_4/f-MWCNT/Ni_2B nanosystem was performed using the energy-dispersive X-ray spectroscopy (EDX) technique (Fig. 5). The SEM-based EDX spectrum of the Fe_3O_4/f-MWCNT/Ni_2B nanocomposite revealed the presence of carbon, oxygen, ferrite, nickel, and boron, along with their corresponding atomic ratios (%), which confirmed that the desired nanostructure has been synthesized. The analysis indicated 26.27 w% C, 23.33 w% O, 41.31 w% Fe, 6.03 w% Ni, and 3.06 w% B in the structure. Furthermore, all the elements were ascertained in Fe_3O_4/f-MWCNT/Ni_2B by SEM-based dot-mapping analysis with corresponding intensities to EDX analysis (Fig. 6). Also, the homogeneity of element distribution is observed by the results of the elemental mapping, corroborating the FESEM and HRTEM analyses.

3.2.5 HRTEM and SAED analysis. The structural morphology, microstructure, and average sizes of the as-synthesized Fe_3O_4/f-MWCNT/Ni_2B nanocomposite were also investigated using high-resolution transmission electron microscopy (HRTEM). The high-resolution TEM (HRTEM) analysis was employed to further characterize the structure of the synthesized Fe_3O_4/f-MWCNT/Ni_2B nanocomposite system. The HRTEM image of Fe_3O_4/f-MWCNT/Ni_2B (Fig. 7) indicates

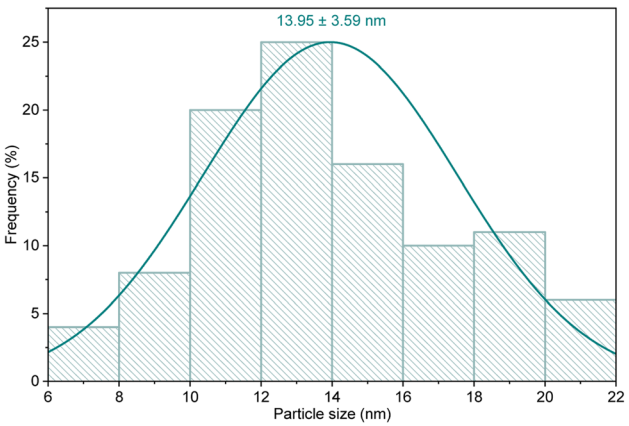

N total	Mean (nm)	SD	Min (nm)	Max (nm)
100	13.94912	3.58966	7.316	21.722

Fig. 8 DLS particle size distribution of as-synthesized Fe_3O_4/f-MWCNT/Ni_2B nanocomposites.

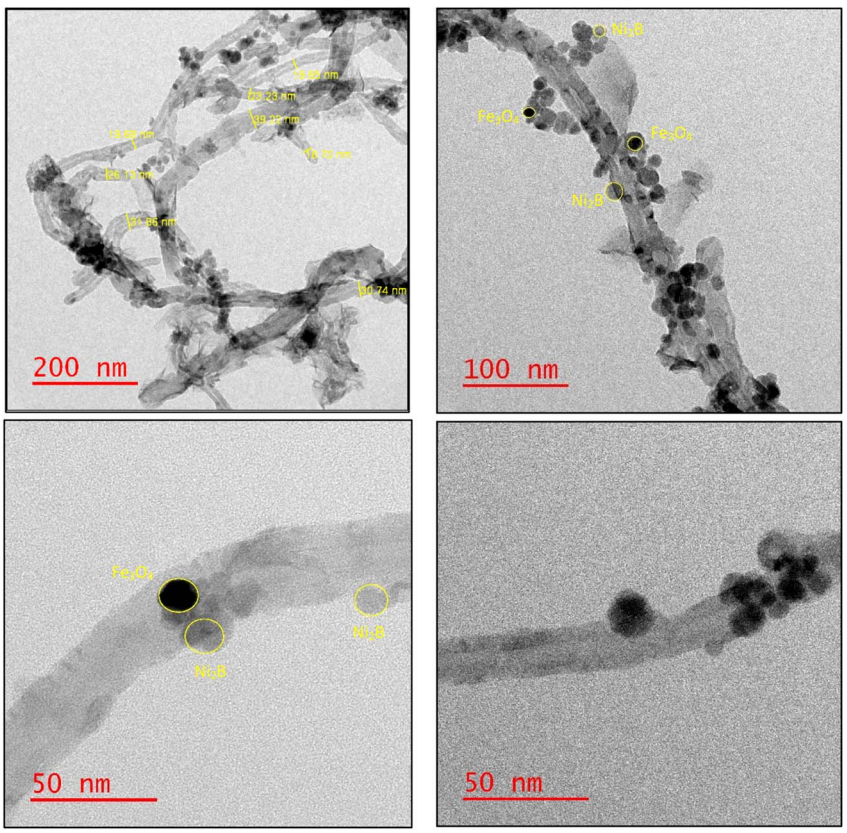

Fig. 7 HRTEM image of as-synthesized Fe_3O_4/f-MWCNT/Ni_2B nanocomposites.

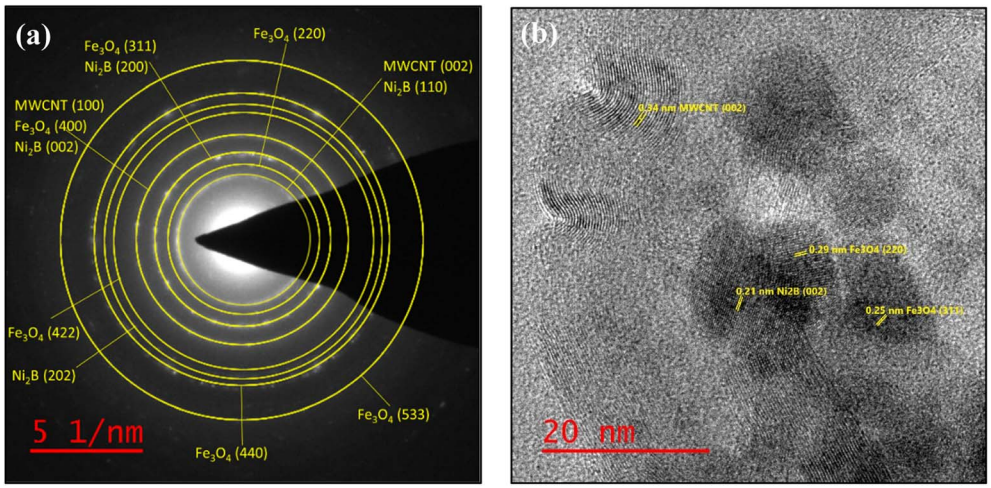

Fig. 9 (a) SAED pattern of the as-synthesized Fe_3O_4/f-MWCNT/Ni_2B nanocomposite and (b) HRTEM micrograph at scale 20 nm and inset lattice fringe.

Table 2 SAED data of Fe_3O_4/f-MWCNT/Ni_2B nanocomposites

No.	Pos. [2Th]	r (nm^{-1})	d-spacing [nm]	Phase	[hkl]
1	26.2734	2.9105	0.339209	MWCNTs	[002]
				Ni_2B	[110]
2	30.4956	3.368	0.293139	Fe_3O_4	[220]
3	35.8109	3.9241	0.250754	Fe_3O_4	[311]
				Ni_2B	[200]
4	43.3896	4.7949	0.208552	Fe_3O_4	[400]
				Ni_2B	[002]
				MWCNTs	[100]
5	53.9317	5.7795	0.170012	Fe_3O_4	[422]
6	60.4985	6.5374	0.152903	Ni_2B	[202]
7	62.9884	6.7835	0.147573	Fe_3O_4	[440]
8	74.9333	7.9384	0.126632	Fe_3O_4	[533]

that the Fe_3O_4 and Ni_2B have been effectively distributed on the outer wall of MWCNT-COOH. In addition, a dark-colored core of Fe_3O_4 nanoparticles, a semi-dark-colored core of Ni_2B nanoparticles, and a light-colored substrate of multi-walled carbon nanotubes were observed for the synthesized nanocomposite system. To achieve a more accurate assessment of particle size, the DLS histogram depicting the distribution of nanoparticles based on the TEM images was plotted (Fig. 8). The multi-walled carbon nanotubes and nanoparticles exhibited mean diameters of approximately 26.15 ± 7.29 nm and 13.95 ± 3.59 nm, respectively. As can be seen, the preponderance of nanoparticles in the nanocomposite system measures between 12 and 14 nm in size.

The selected area electron diffraction (SAED) patterns for the synthesized Fe_3O_4/f-MWCNT/Ni_2B nanocomposite consist of typical polycrystalline diffraction rings, suggesting a nanocrystalline structure (Fig. 9a). In accordance with the SAED pattern, bright rings attributed to magnetite, Ni_2B, and MWCNT phases confirm the formation of a nanocomposite system. The identification of the phases was accomplished by determining the diameter and d-spacing of each ring, which exhibited lattice fringe spacing values consistent with those determined using XRD. Two distinct concentric rings that represent the (002) and (100) planes in the patterns can be used to identify the MWCNT phase. Furthermore, six other strong diffraction rings were assigned to the diffraction plan of pure cubic Fe_3O_4 and Ni_2B phases. The statistical data obtained from this analysis are summarized in Table 2. Lattice-structured nanoparticles and the interlayer spacing can be seen in this nano-polycrystalline Fe_3O_4/f-MWCNT/Ni_2B HRTEM micrograph (Fig. 9b). Analysis of this micrograph indicates that clear fringes of the MWCNT phase with the distance of 0.34 nm (diffraction peaks at 26.27° in the XRD pattern) corresponding to the (002) planes possess fingerprint-like orientations, which is a phenomenon that has been reported previously.[82] The (220) and (311) crystal facets of cubic phase Fe_3O_4 (diffraction peaks at 30.49° and 35.81° in the XRD pattern), are observed, as well as interlayer spacing corresponding to the (002) planes of the Ni_2B phase (diffraction peak at 43.39° in the XRD pattern) with a lattice fringe spacing of 0.21 nm. All these pieces of evidence substantiate the generation of the Fe_3O_4/f-MWCNT/Ni_2B nanocomposite system.

3.2.6 XPS analysis. X-ray photoelectron spectroscopy (XPS) is an impressive surface analysis technique that provides accurate insights into the chemical composition, purity, and oxidation states of elements. During the XPS analysis of the as-prepared Fe_3O_4/f-MWCNT/Ni_2B nanocomposite survey scan, all the elements of the nanocomposite were observed to be present on its surface, as confirmed by the EDX analysis. The XPS narrow scans and the deconvolution peaks of Ni 2p (858.67 eV), Fe 2p (712.08 eV), O 1s (532.27 eV), C 1s (285.14 eV), and B 1s (192.76 eV)[83] are demonstrated in Fig. 10 and surface elemental analysis of the as-prepared nanocomposite s is tabulated in their spectra. In the (C 1s) XP spectrum of the Fe_3O_4/f-MWCNT/Ni_2B, five well-defined deconvoluted peaks are evident, corresponding to the functional groups including C=C sp^2 (284.67 eV), C–C/C–H (284.88 eV), C–O (285.62 eV), and C=O (286.4 eV) in aligning well with literature reports for MWCNTs.[84] Also, the peak observed at 288.9 eV is believed to be a result of π–π interactions found in the carbon rings of the MWCNT

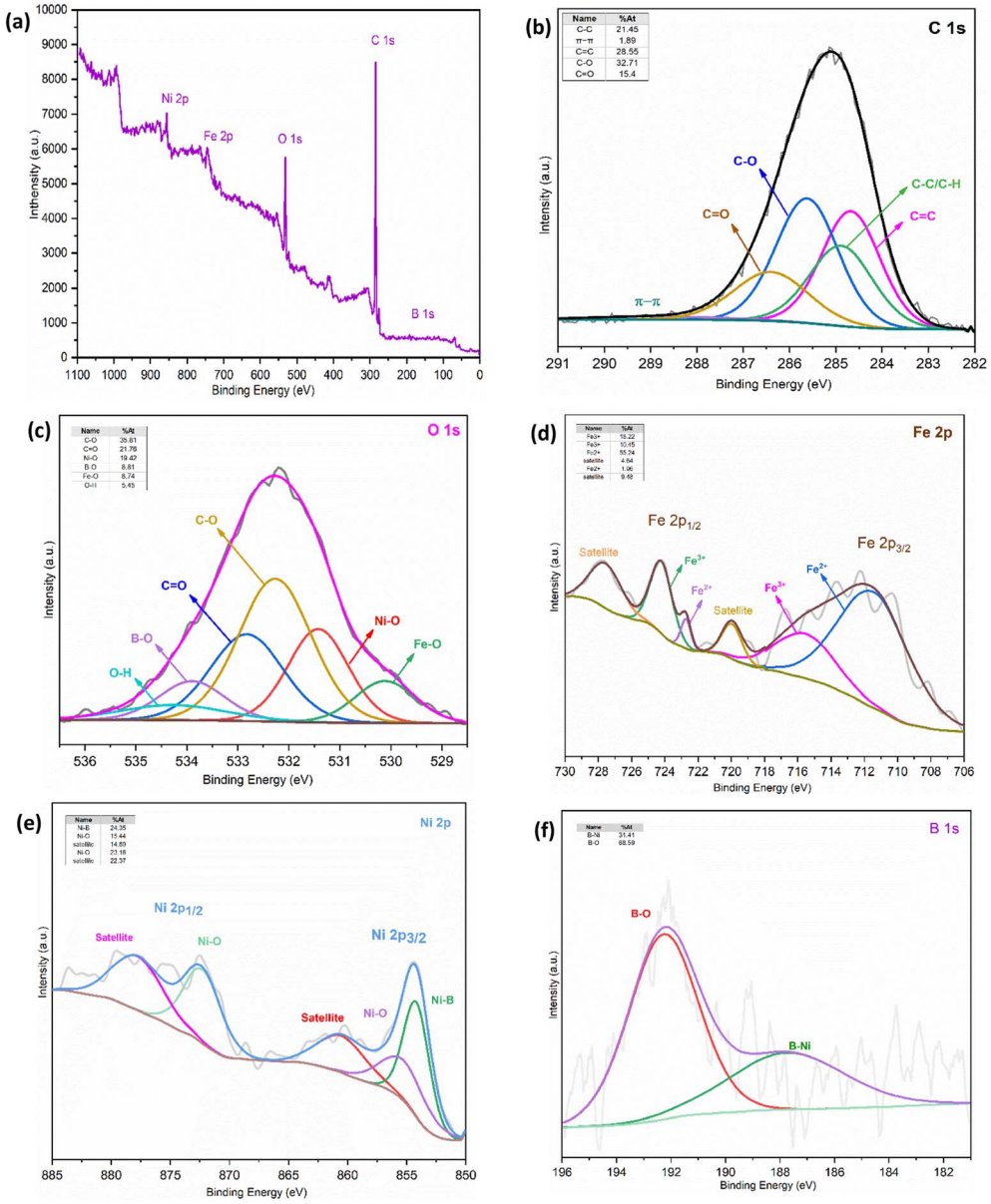

Fig. 10 (a) XPS survey spectrum of Fe_3O_4/f-MWCNT/Ni_2B and high-resolution XPS spectra of (b) C 1s, (c) O 1s, (d) Fe 2p, (e) Ni 2p, and (f) B 1s.

structure.[85] The finding data suggest that the desired nanocomposite contains MWCNTs-COOH. Based on the NIST XPS database, in the detailed deconvoluted peaks of the Fe 2p doublet, the peaks at binding energies (BEs) of 724.26 and 711.89 eV are unequivocally allocated to Fe $2p_{1/2}$ and Fe $2p_{3/2}$ spin-orbits, respectively.[86] After curve fitting of Fe $2p_{1/2}$ and Fe $2p_{3/2}$, the two clearly distinguishable peaks confirm the existence of both +2 and +3 oxidation states for Fe. The two peaks at 710.45 and 722.73 eV can be attributed to the characteristic peaks Fe $2p_{3/2}$ and Fe $2p_{1/2}$ of Fe^{2+}, and those at 715.55 and 724.2 eV are characteristic peaks Fe $2p_{3/2}$ and Fe $2p_{1/2}$ of Fe^{3+}. The satellite peaks observed at 720.03 and 727.65 eV can serve as an indication of the purity and existence of the Fe_3O_4 phase as well as further confirm the predominance of Fe^{3+} high-spin chemical valence in the as-prepared Fe_3O_4/f-MWCNT/Ni_2B nanocomposite. The relaxation of valence electrons at the 2p level induces a configuration interaction in Fe^{3+} and generates satellite peaks.[87] Deconvolution of Ni 2p XPS peaks showed the major peak located at 854.17 eV related to Ni–B bonds.[88] Similarly, the peaks observed at 855.2 and 872.28 eV correspond to Ni^{2+} $2p_{3/2}$ and Ni $2p_{1/2}$, respectively, indicating the existence of either NiO or $Ni(OH)_2$ which might have resulted from the preservation and washing of the as-synthesized nanocomposite in the atmosphere.[88,89] It can be inferred that the surface of Ni_2B is covered by a thin layer comprising hydroxide $Ni(OH)_2$ or oxide NiO.[89,90] This hypothesis requires further studies to confirm its validity. Satellite peaks were also observed at 860.51 and 877.77 eV.[91] Additionally, the high-resolution XPS spectra of B 1s show two peaks at 187.82 and 192.41 eV, which are assigned to the Ni–B bond and boron linked to oxygen species. The reference XPS spectra of Ni_2B revealed that the Ni_2B undergoes oxidation to B_2O_3, indicated by a B 1s at 192.41 eV and

Table 3 Results of BET analysis for the as-prepared nanocomposite system[a]

Sample	S_{BET} [$m^2\ g^{-1}$]	V_m [$cm_{(STP)}^3\ g^{-1}$]	Average pore diameter [nm]	Total pore volume [$cm^3\ g^{-1}$]	V_p [$cm^3\ g^{-1}$]
Fe_3O_4/f-MWCNT	136.53	31.369	13.643	0.4657	0.4469
Fe_3O_4/f-MWCNT/Ni_2B	97.334↓	22.363↓	18.156↑	0.4418↓	0.4313↓

[a] S_{BET}: Brunauer–Emmett–Teller surface area. V_m: Brunauer–Emmett–Teller volume of monolayer coverage. V_p: BJH desorption cumulative volume of pores.

a prominent peak in the O 1s core level at 533.9 eV. It is uncertain whether the particles are situated inside the nanoparticles or in their vicinity.[80,88,91b] Furthermore, the XPS results indicate that the obtained Ni : B molar ratio (1.968) agrees with the results obtained from the EDX analysis. In the O 1s orbital X-ray photoelectron spectrum, distinct bands are observed at 530.11, 531.42, 532.27, 532.82, and 533.9 eV energies, corresponding to binding energies (BEs) of lattice O associated with O–Fe, O–Ni, C–O, and B–O respectively. Furthermore, the peak at 534.27 eV corresponds to surface hydroxyl groups on magnetic MWCNTs.[92] Therefore, based on the data presented, the appearance of the Ni and B peaks was the most effective evidence that Ni_2B was supported on the surface of these prepared Fe_3O_4/f-MWCNT/Ni_2B nanocatalysts.

3.2.7 BET analysis. With the aim of deeply investigating the specific surface area and porosity of the synthesized Fe_3O_4/f-MWCNT/Ni_2B nanocomposite system, the Brunauer–Emmett–Teller (BET) surface areas of Fe_3O_4/f-MWCNT and Fe_3O_4/f-MWCNT/Ni_2B were assessed by applying the N_2 adsorption–desorption isotherm at 77 K.[93] The obtained results are tabulated in Table 3. As shown in Fig. 11a and b, consistent with the BDDT IUPAC classification the shape of the N_2 adsorption–desorption isotherm for the prepared samples belongs to IV-like isotherm[71g,94] due to the intratubular structure and capillary condensation, with an H_3 loop of hysteresis. This suggests the presence of a micro- and mesoporous structure in the material.[95] It is evident that low gas adsorption at low relative pressures and the negligible alterations in pore volume implied a low micropore volume. Subsequently, increasing the relative pressure above 0.9 results in a significant escalation of gas adsorption after the initial saturation of micropores serving evidence for the presence of a mesoporous structure.[95,96] Additionally, the knee position is observed in the N_2 adsorption–desorption isotherm for Fe_3O_4/f-MWCNT and Fe_3O_4/f-MWCNT/

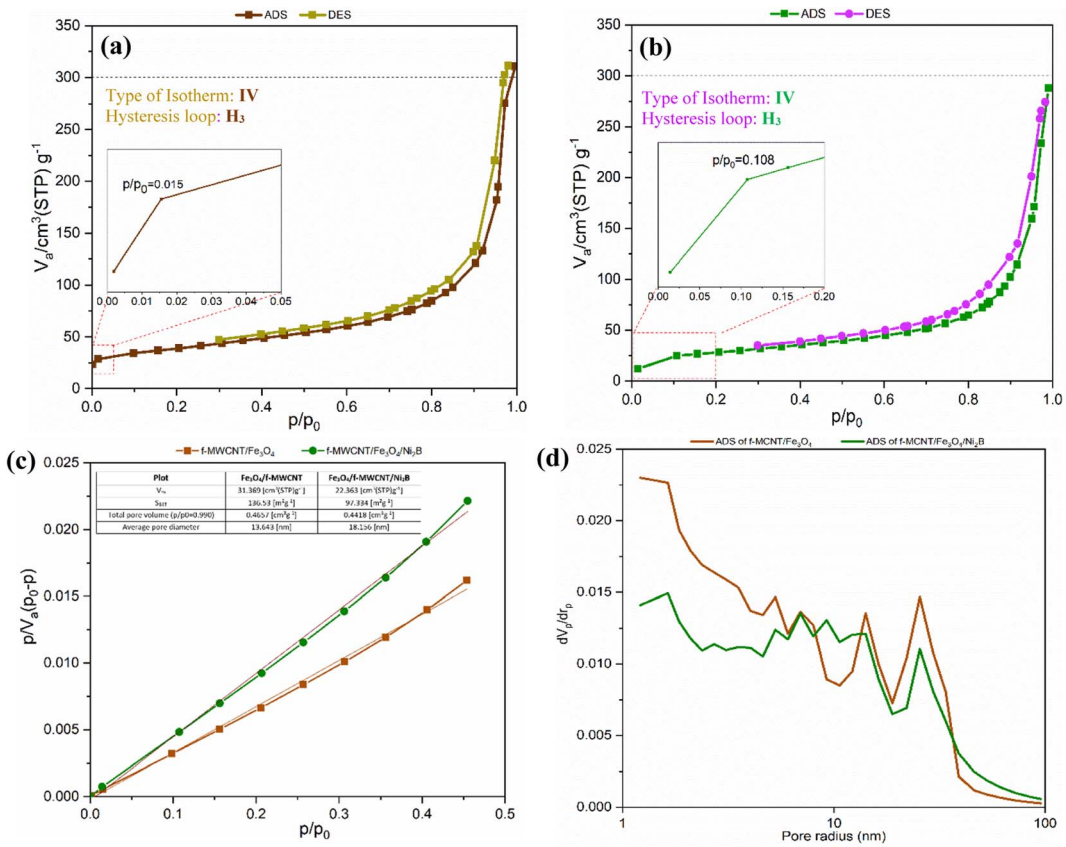

Fig. 11 N_2 adsorption–desorption isotherms of (a) Fe_3O_4/f-MWCNT and (b) Fe_3O_4/f-MWCNT/Ni_2B at 77 K. (c) Brunauer–Emmett–Teller (BET) isotherm and (d) Barrett–Joyner–Halenda (BJH) pore size distribution isotherm.

Ni_2B at relative pressures of 0.015 and 0.108, respectively. The knee position, which is established at the relative pressure of the completion of monolayer coating and the inception of multilayer adsorption, represents the monolayer capacity.[97] Evidently, the as-prepared nanocomposite system compared to Fe_3O_4/f-MWCNT exhibited the knee point at higher relative pressure, likely due to the increase in the pore size of the examined system. On the other hand, as can be observed in Table 3, Fig. 11b and c, modifying Fe_3O_4/f-MWCNT by Ni_2B and synthesizing the Fe_3O_4/f-MWCNT/Ni_2B nanocomposite system resulted in a decrease of the Brunauer–Emmett–Teller (BET) surface area from 136.53 $m^2\ g^{-1}$ to 97.334 $m^2\ g^{-1}$, along with a slight decrease in pore volume (V_{total}) from 0.4657 $cm^3\ g^{-1}$ to 0.4418 $cm^3\ g^{-1}$. The observed decreases in specific surface area and pore volume can be ascribed to the presence of Fe_3O_4 and Ni_2B on multi-walled carbon nanotube surfaces and the blockage of pores in MWCNT-COOH, indicating the successful embedding of nanoparticles inside the pores.[95,96a] Meanwhile, the pore size increased from 13.643 nm to 18.156 nm after loading the Ni_2B nanoparticles. The increase in the pore diameter (pore size) can most probably be attributed to the additional volume introduced by Ni_2B on the surface of Fe_3O_4/f-MWCNT. Overall, the obtained results confirm the successful synthesis of the Fe_3O_4/f-MWCNT/Ni_2B nanocatalyst. It is noteworthy that by including surface changes in the modified system, the catalytic performance of the as-prepared nanocomposite has been significantly impacted.

3.2.8 Thermal gravimetric analysis. In this research, thermal gravimetric analysis (TGA) and differential thermal gravimetric (DTG) were conducted under an N_2 atmosphere in the temperature range of 0–800 °C, to check the thermal behavior and stability of the as-synthesized nanocomposite system (Fig. 12). The obtained outcomes provide valuable insights into the thermal stability and decomposition behavior of the investigated system. It is clear from the TGA thermogram that for the Fe_3O_4/f-MWCNT/Ni_2B nanocomposite, there are three steps of mass losses at temperatures of 0–430, 430–550, and 550–750 °C. In the initial stage, the mass loss (1.72%) is due to the decomposition of organic moieties such as the surface hydroxyl groups and physically adsorbed water or trapped solvents utilized during the nanocomposite formation processes.[98] In the second step, the weight loss (5.13%) is mainly associated with the decomposition of Ni_2B and also is corresponding to the thermal decomposition of the Fe_3O_4. In the final stage, the weight loss (6.73%) is attributed to the pyrolysis and degradation of the MWCNT network.[82c] Meanwhile, the DTA diagram indicated that the Fe_3O_4/f-MWCNT/Ni_2B system exhibits sufficient thermal stability to withstand elevated temperature conditions of up to 369 °C, with only a weight loss of 1.72%.

3.2.9 VSM analysis. A crucial aspect that plays a vital role in the practical application of nanocomposites is their ability to be effectively separated and recycled from the reaction medium, which requires having desirable magnetic properties. Hence, to investigate the magnetic properties of the synthesized nanocatalyst, a vibrating sample magnetometer (VSM) analysis was carried out in an external magnetic field up to 20 kOe at room temperature. Fig. 13 illustrates the magnetic response of Fe_3O_4, Fe_3O_4/f-MWCNT, and Fe_3O_4/f-MWCNT/Ni_2B at room temperature. As demonstrated in the VSM graph, the saturation magnetization values (M_s) of Fe_3O_4, Fe_3O_4/f-MWCNT, and Fe_3O_4/f-MWCNT/Ni_2B were measured to be 75.71, 46.51, and

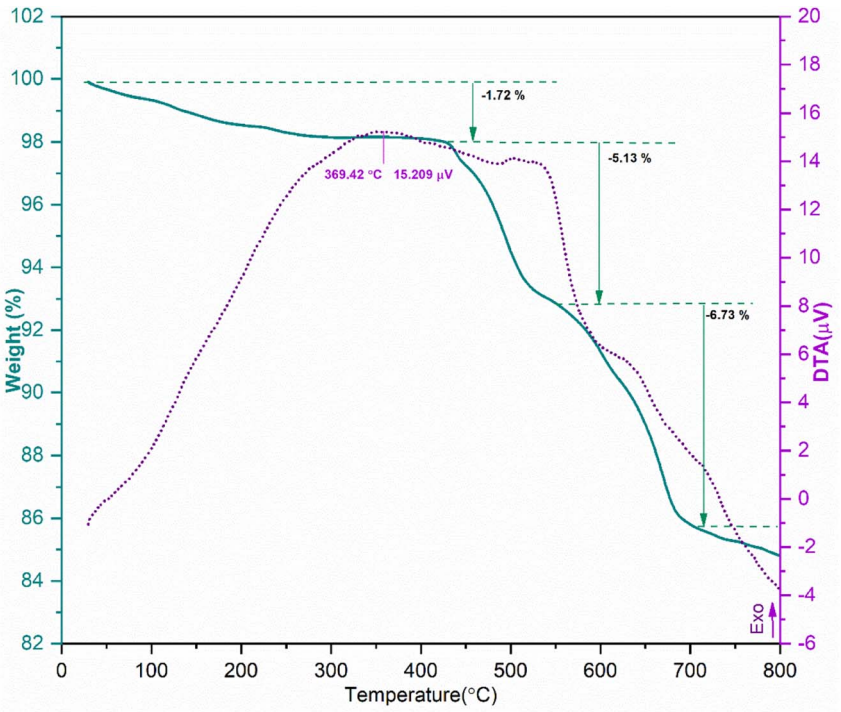

Fig. 12 TGA/DTA diagram of the Fe_3O_4/f-MWCNT/Ni_2B nanocomposite.

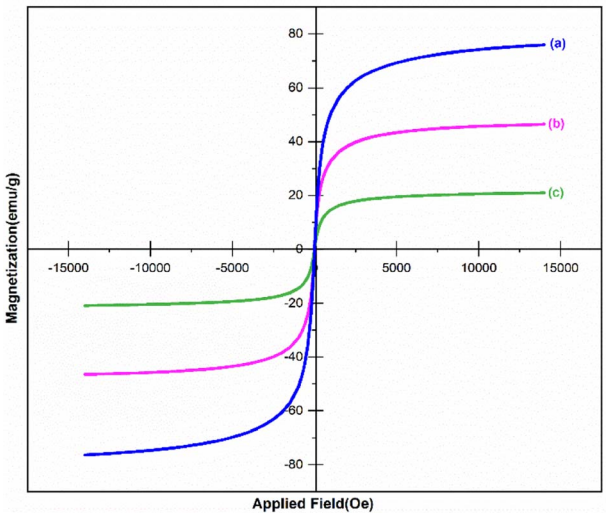

Fig. 13 VSM magnetization diagram of (a) Fe_3O_4, (b) Fe_3O_4/f-MWCNT, and (c) Fe_3O_4/f-MWCNT/Ni_2B nanocomposites.

21.05 emu g^{-1}, respectively. This decrease in saturation magnetization of Fe_3O_4/f-MWCNT/Ni_2B can be attributed to the presence of nonmagnetic amorphous coatings of f-MWCNTs and Ni_2B in the matrix of the examined sample. Notwithstanding the diminished saturation magnetizations (M_s), the as-synthesized nanocomposite system still demonstrates noteworthy magnetic properties, which enables its recovery from the aqueous solution using an external magnet. In addition, the absence of a hysteresis loop confirmed that all the above-examined samples have a notable paramagnetism behavior.

3.3 Evaluation of catalytic performance of the Fe_3O_4/f-MWCNT/Ni_2B nanocatalyst for the synthesis of 1,4-benzodiazepines

3.3.1 Optimization of reaction conditions. In this research, after catalyst characterization, for the synthesis of target products, the catalytic performance of the as-prepared Fe_3O_4/f-MWCNT/Ni_2B nanocomposite was investigated in the one-pot synthesis of 1,4-benzodiazepines *via* the three-component

Table 4 Optimization of the reaction conditions for the one-pot three-component synthesis of 3,3-dimethyl-11-phenyl-2,3,4,5,10,11-hexahydro-1*H*-dibenzo[*b*,*e*][1,4]diazepin-1-one

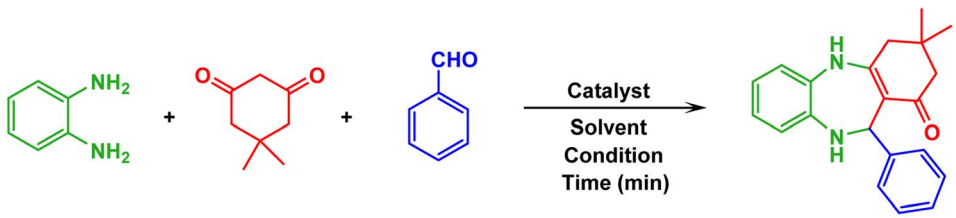

1 2 3a 4a

Entry[a]	Catalyst	Catalyst loading (mg)	Solvent	Condition	Time (min)	Conversion (%)
1	Fe_3O_4/f-MWCNT/Ni_2B	15	MeOH	Reflux	180	—
2	Fe_3O_4/f-MWCNT/Ni_2B	15	EtOH	Reflux	180	—
3	Fe_3O_4/f-MWCNT/Ni_2B	15	EtOAc	Reflux	180	—
4	Fe_3O_4/f-MWCNT/Ni_2B	15	CH_2Cl_2	Reflux	180	—
5	Fe_3O_4/f-MWCNT/Ni_2B	15	CH_3CN	Reflux	180	—
6	Fe_3O_4/f-MWCNT/Ni_2B	15	H_2O	r.t.	180	30
7	Fe_3O_4/f-MWCNT/Ni_2B	15	H_2O	Reflux	90	100
8	Fe_3O_4/f-MWCNT/Ni_2B	15	H_2O : EtOH (1 : 1)	70 °C	180	60
9	Fe_3O_4/f-MWCNT/Ni_2B	10	H_2O	US/60 °C	180	60
10	Fe_3O_4/f-MWCNT/Ni_2B	10	EG	US/60 °C	40	100
11	**Fe_3O_4/f-MWCNT/Ni_2B**	**10**	**PEG-400**	**US/60 °C**	**30**	**100**
12	Fe_3O_4/f-MWCNT/Ni_2B	15	PEG-400	US/60 °C	30	100
13	Fe_3O_4/f-MWCNT/Ni_2B	10	PEG-400	60 °C	180	70
14	Fe_3O_4/f-MWCNT/Ni_2B	10	PEG-400	US/ice bath	180	—
15	Fe_3O_4/f-MWCNT/Ni_2B	7	PEG-400	US/60 °C	100	100
16	Fe_3O_4/f-MWCNT/Ni_2B	5	PEG-400	US/60 °C	180	80
17	Fe_3O_4/f-MWCNT/Ni_2B	10	—	US/60 °C	180	—
18	f-MWCNT	10	PEG-400	US/60 °C	180	—
19	Fe_3O_4	10	PEG-400	US/60 °C	180	—
20	Ni_2B	10	PEG-400	US/60 °C	180	—
21	Fe_3O_4/f-MWCNT	10	PEG-400	US/60 °C	180	—
22	Fe_3O_4/Ni_2B	10	PEG-400	US/60 °C	180	—
23	—	—	PEG-400	US/60 °C	180	—

[a] All reactions were carried out with *o*-phenylenediamine (1 mmol), dimedone (1 mmol), and benzaldehyde (1 mmol), in 3 mL solvent.

condensation reaction of *o*-phenylenediamine (**1**), dimedone (**2**), and various aliphatic/aromatic/heteroaromatic aldehydes (**3a–o**). The scrutiny of the reaction condition optimization for the synthesis of 3,3-dimethyl-11-phenyl-2,3,4,5,10,11-hexahydro-1*H*-dibenzo[*b*,*e*][1,4]diazepin-1-one (**4a**) through a one-pot three-component reaction of *o*-phenylenediamine (**1**) and dimedone (**2**) with benzaldehyde (**3a**) in the presence of the as-prepared Fe_3O_4/f-MWCNT/Ni_2B nanocomposite system as a model reaction was conducted (Table 4). The effect of variables including several solvents, the amount of the catalyst, and temperature was studied.

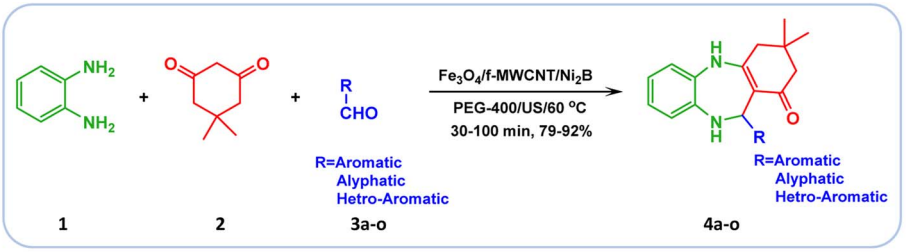

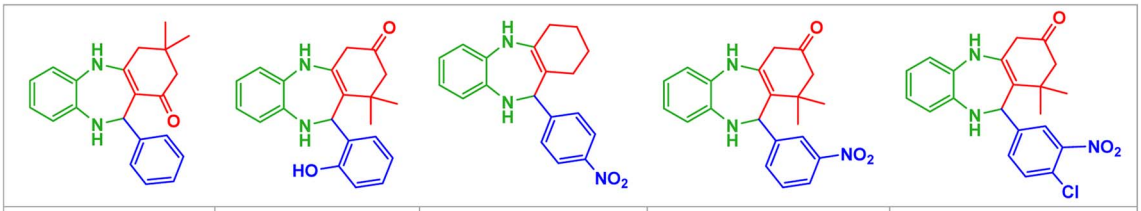

4a, T= 30 min, Y= 83% M_p= 245-246 °C TON= 80.5825 TOF= 2.6861 min^{-1}	**4b**, T=90 min, Y= 79% M_p= 202 °C TON= 76.6990 TOF= 0.8522 min^{-1}	**4c**, T= 20 min, Y= 91% M_p= 274 °C TON= 88.3495 TOF=4.4175 min^{-1}	**4d**, T= 30 min, Y= 90% M_p= 147 °C TON=87.3786 TOF=2.9126 min^{-1}	**4e**, T= 20, Y= 91% M_p= 196 °C TON=88.3495 TOF=4.4175 min^{-1}
4f, T= 25 min, Y= 89% M_p= 233 °C TON= 86.4078 TOF=3.4563 min^{-1}	**4g**, T= 35 min, Y= 88% M_p= 234 °C TON= 85.4369 TOF= 2.4411 min^{-1}	**4h**, T= 48 min, Y= 83% M_p= 231 °C TON= 80.5825 TOF= 1.6788 min^{-1}	**4i**, T= 57 min, Y= 87% M_p= 250 °C TON= 84.4660 TOF= 1.4819 min^{-1}	**4j**, T= 57 min, Y= 88% M_p= 252 °C TON= 85.4369 TOF= 1.4989 min^{-1}
4k, T= 67 min, Y= 89% M_p= 135-136 °C TON= 86.4078 TOF= 1.2897 min^{-1}	**4l**, T= 40 min, Y= 88% M_p= 175-177 °C TON= 85.4369 TOF= 2.1359 min^{-1}	**4m**, T= 50 min, Y= 83% M_p= 243 °C TON= 80.5825 TOF= 1.6116 min^{-1}	**4n**, T= 55 min, Y= 80% M_p= 244-245 °C TON= 77.6699 TOF= 1.4122 min^{-1}	**4o**, T= 40 min, Y= 91% M_p= 219-220 °C TON= 88.3495 TOF=2.2087 min^{-1}

All reactions were carried out in 3 mL of polyethylene glycol 400.
Y= Yield, T=Time, M_p=Melting point
TON (turnover number) = [(mol of product) / (mol of catalyst)]
TOF (turnover frequency) = [(mol of product) / (mol of catalyst) × (time)]
The TONs and TOFs value were calculated based on the existed amount of nickel in the as-prepared nanocomposite.
(1n 10 mg of the nanocomposite, 0.603 mg or 0.0103 mmol of Ni has existed).

Scheme 3 One-pot synthesis of 1,4-benzodiazepines in the presence of Fe_3O_4/f-MWCNT/Ni_2B nanocomposites.

To find a suitable solvent, a model reaction was carried out with 10 and 15 mg of the Fe_3O_4/f-MWCNT/Ni_2B nanocatalyst in several solvents including methanol (CH_3OH), ethanol (CH_3-CH_2OH), ethyl acetate (EtOAc), acetonitrile (CH_3CN), dichloromethane (CH_2Cl_2), water (H_2O), ethylene glycol (EG), and polyethylene glycol (PEG-400) also under solvent-free conditions. In the presence of the aforementioned nanocatalyst, the reaction is efficiently accomplished with high yield using water (H_2O), polyethylene glycol (PEG-400), and ethylene glycol (EG) solvents. However, it is noteworthy that when employing water (H_2O) (Table 4, entry 7) and ethylene glycol (EG) (Table 4, entry 10) as a solvent, the reaction time is prolonged in comparison to polyethylene glycol (PEG-400) (Table 4, entry 11) as a solvent. Therefore, the outperformance was attained when polyethylene glycol (PEG-400) was used as an optimum solvent compared with the studied solvents for this reaction. In follow-up research, the model reaction was carried out with different amounts of the as-prepared Fe_3O_4/f-MWCNT/Ni_2B nanocomposite (5–15 mg) in polyethylene glycol (PEG-400) solvent to ascertain the best loading of the nanocatalyst. Based on the information provided in Table 4, in situations whereby the catalyst amount is increased from 10 to 15 mg, the product yield and reaction time remained constant. Conversely, reducing the amount of catalyst from 10 to 5 mg resulted in a decrease in product yield and an increase in reaction time. Thus, 10 mg was found to be the optimal amount for nanocatalyst loading (Table 4, entry 11). Meanwhile, the effect of the reaction temperature was studied at various temperatures under favorable solvent and amount of nanocomposite conditions. The result showed that 60 °C is the best temperature for the reaction in polyethylene glycol (PEG-400) as a solvent. In the end, when the synthesis reaction was carried out under ultrasonication at 60 °C, surpassing the performance of the nanocomposite has been observed compared to non-ultrasonication. Furthermore, to

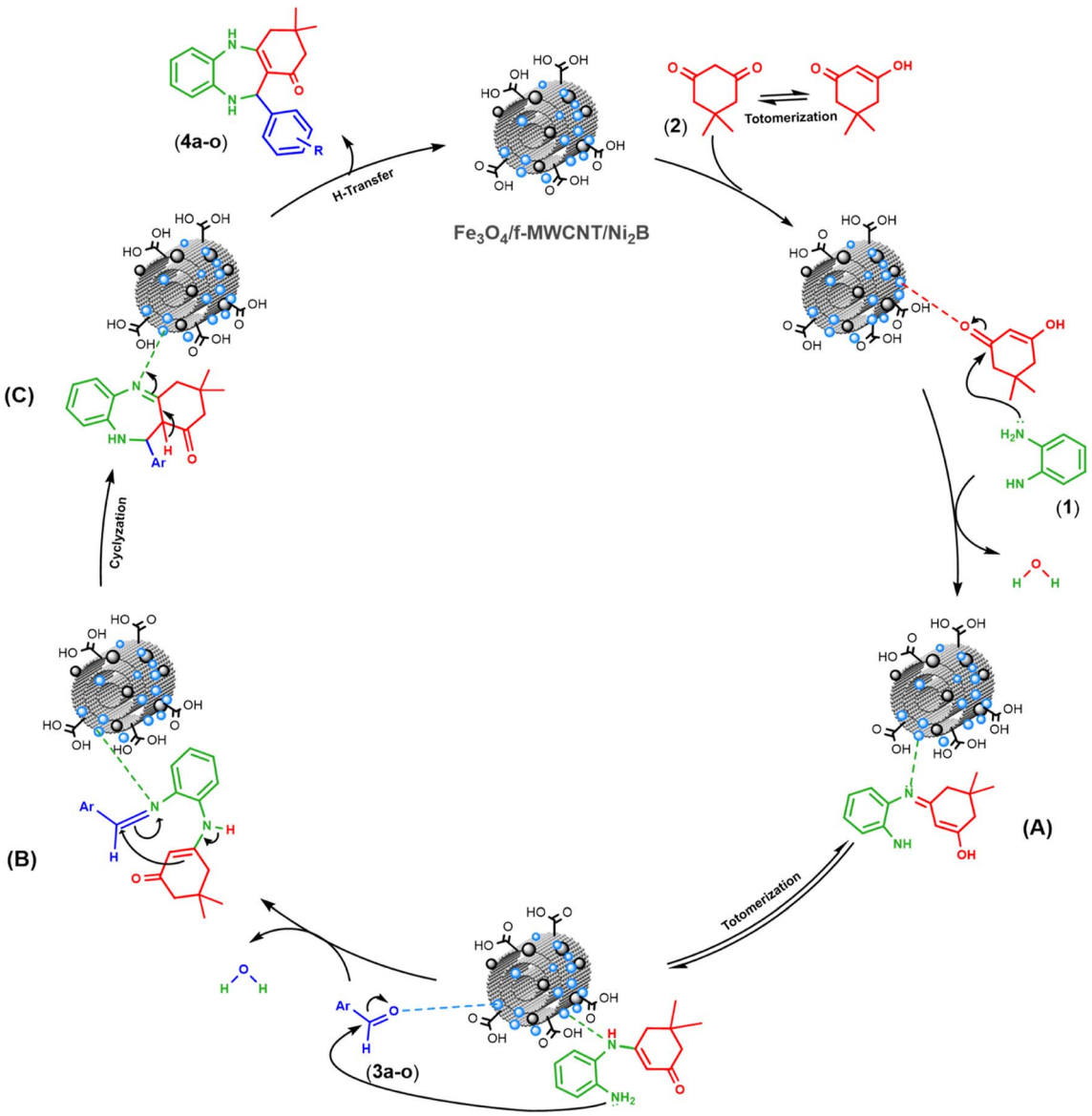

Scheme 4 Plausible mechanism for synthesis of 1,4-benzodiazepines catalyzed by the Fe_3O_4/f-MWCNT/Ni_2B nanocomposite.

investigate the impact of the as-prepared nanocatalyst on the synthesis process of **4a**, a series of control experiments utilizing component parts of the Fe_3O_4/f-MWCNT/Ni_2B nanocomposite (Table 4, entries 17–21) and also without catalyst (Table 4, entry 22) was implemented. Encouragingly, the results of the control experiments unequivocally revealed that the catalytic efficacy of the aforementioned nanocomposite is superior to that of its constituents. Following the optimization of reaction conditions, in order to showcase the application efficiency of the aforementioned new magnetic nanocomposite in organic synthesis, a protocol for the one-pot synthesis of 1,4-benzodiazepine scaffolds was designed. As shown in Scheme 4, the optimized reaction condition was applied to an array of aliphatic/aromatic/heteroaromatic aldehydes (**3a–o**) with electron-donating and electron-withdrawing groups (EDGs and EWGs) in conjunction with *o*-phenylenediamine (**1**) with dimedone (**2**) for the synthesis of a range of the corresponding 1,4-benzodiazepines (**4a–o**). Also, it's obvious that all the substituted aromatic aldehydes along with aliphatic aldehydes have successfully produced the desired products in good-to-excellent yields (79–91%). Notably, the outcomes in Scheme 3 denoted an interesting trend in the chemical reactivity of benzaldehydes. In more explicit terms, the reaction rate of benzaldehydes with electron-withdrawing groups (EWGs) was found to be higher than that observed in the presence of benzaldehydes possessing electron-donating groups (EDGs). Also, the present study aimed to investigate the impact of the substituent position on reaction time and yields. To this end, benzaldehydes possessing functional groups at the *ortho*, *meta*, and *para* positions were utilized to explore this effect. The findings indicated that substitutions on aromatic aldehydes, except for *ortho*-hydroxy benzaldehyde (Scheme 3, **4b**), have an insignificant impact on reaction time and yields. The approach employed in this study was subsequently expanded to both aliphatic aldehydes (Scheme 3, **4m–n**) and heterocyclic aldehydes (Scheme 3, **4o**), leading to the formation of corresponding 1,4-benzodiazepines. Nonetheless, the reaction time for the synthesis of these benzodiazepines was observed to be slightly longer in comparison to other benzaldehydes.

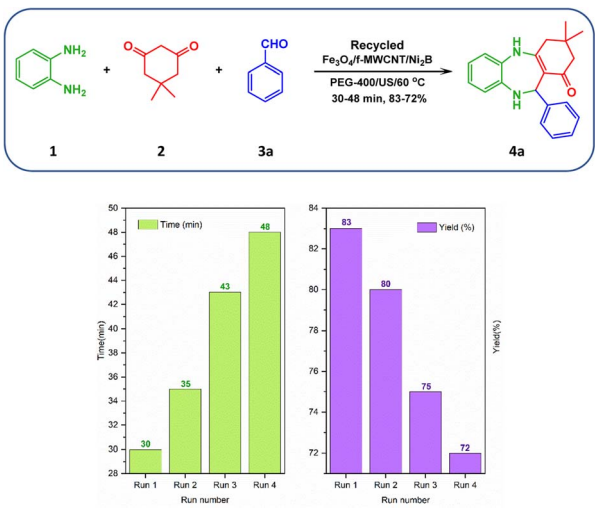

Fig. 14 Reusability diagram of the Fe_3O_4/f-MWCNT/Ni_2B nanocatalyst.

Overall, the obtained result indicated that the as-prepared Fe_3O_4/f-MWCNT/Ni_2B nanocomposite exhibits remarkable catalytic activity with an excellent turnover number (TON) and turnover frequency (TOF) in the production process of 1,4-benzodiazepines. The TOF value serves as an indicator of the catalytic performance per active site of catalysts. An excellent TOF value is a reflection of the inherent property of the catalysts to provide superior performance.

3.3.2 Proposed reaction mechanism. This research outlines, a plausible mechanism[99] for the one-pot synthesis of 1,4-benzodiazepines utilizing the as-prepared Fe_3O_4/f-MWCNT/Ni_2B nanocomposite. Scheme 4 revealed the crucial role of catalysis in each step of the reaction, for the formation of C–C bond coupling and cyclization. The as-prepared Fe_3O_4/f-MWCNT/Ni_2B nanocomposite has been able to activate the carbonyl and imine groups and streamline the coupling of C–C and C–N bonds.

The first interaction occurs between one of the oxygen atoms of dimedone with the active sites on the as-prepared nanocomposite surface. Consequently, the nanosystem activates the

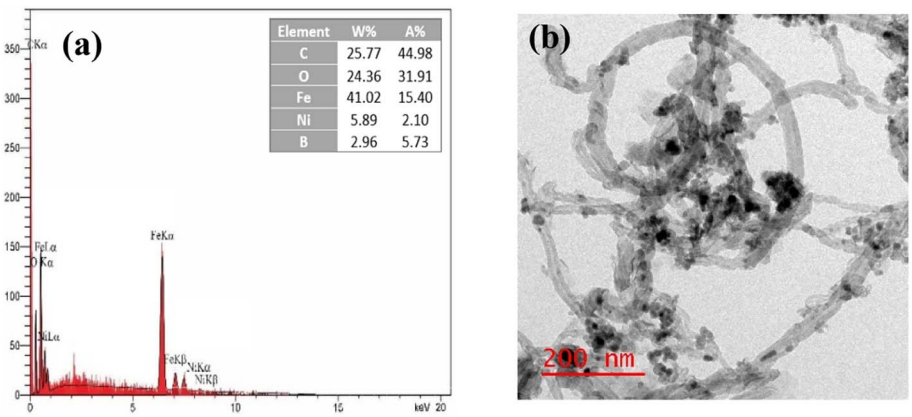

Fig. 15 (a) EDX analysis of the Fe_3O_4/f-MWCNT/Ni_2B nanocatalyst after 4 cycles and (b) TEM image of the Fe_3O_4/f-MWCNT/Ni_2B nanocatalyst after 4 cycles.

Table 5 Comparison of the catalytic activity of the Fe_3O_4/f-MWCNT/Ni_2B nanocomposite with some reported catalysts for the synthesis of 1,4-benzodiazepines

No.	Catalyst and reaction conditions	Time (min)	Yield (%)	Ref.
1	**Fe_3O_4/f-MWCNT/Ni_2B (10 mg), PEG-400, US/60 °C**	**30**	**92**	**This work**
2	Fe_3O_4@chitosan (40 mg), EtOH, r.t.	120	91	60
3	La_2O_3 (0.01 eq.), H_2O, 60 °C	4 h	81	33
4	$La(OH)_3$ (0.01 eq.), H_2O, 60 °C	3.5 h	76	33
5	SPINOL-derived chiral phosphoric acid (100 mg), 1,4-dioxane, 40 °C	17 h	85	54
6	Oxalic acid (40% mol), H_2O, reflux	120	88	55
7	L-Proline (20% mol), H_2O, 60 °C	100	86	40
8	Gr@TiO_2 NCs (140 mg), EtOH, 20 °C	79	92	35
9	[H-PFBA][PF_6] (80 mg), CH_2Cl_2, 40 °C	35	95	46
10	UiO-66 (6 mg), solvent-free, r.t.	45	89	31
11	Chitosan@triacid imide (7 mg), EtOH, r.t.	50	87	52
12	CeO_2/CuO@N-GQDs@NH_2 (5 mg), EtOH, r.t.	30	94	45
13	$B(HSO_4)_3$ (100 mg), EtOH–H_2O, reflux	30	85	39
14	ZnS nanoparticles (10% mol), EtOH, reflux	19	85	48
15	$CoFe_2O_4$@GO-K 22, Ni (3 mg), H_2O, 60 °C	10	95	43
16	Cu@PI-COF (20 mg), solvent free, MW/180w	5	93	36
17	GO nanosheet (15 mg), water, 70 °C	30	95	34

carbonyl group of dimedone. Subsequently, one of the NH_2 groups of *o*-phenylenediamine (**1**) undergoes an addition reaction and attacks the nanocatalyst-activated carbonyl group of dimedone (**2**). This leads to the elimination of a molecule of H_2O and the formation of the nucleophilic addition–elimination product with an enamine structure (**A**). Following this, a hydrogen transfer takes place, resulting in the conversion of the enamine structure into its tautomeric counterpart. Next, the other amino group of the tautomeric form of the enamine intermediate (**A**) reacts with the carbonyl group of aldehydes (**3a–o**), which is activated by the nanocomposite, forming an intermediate imine–enamine through dehydration (**B**). Ultimately, the targeted intermediate (**C**) is formed *via* the coupling of C–C bond and the cyclization of the intermediate, aided by the nanocatalyst. The final benzodiazepines (**4a–o**) are acquired by transferring a proton, and the magnetic nanocatalyst is isolated for ensuing recycling. Overall, these results provide insights into the proposed mechanism for the synthesis of 1,4-benzodiazepines utilizing as-prepared Fe_3O_4/f-MWCNT/Ni_2B nanocomposite.

3.3.3 Reusability of the Fe_3O_4/f-MWCNT/Ni_2B nanocatalyst. Some of the most important economic and green chemistry parameters of applying catalysts in organic synthesis for commercial and industrial applications are their potential recyclability and high stability moieties on their surface. In order to study this, in this research, the recoverability and reusability of the as-prepared Fe_3O_4/f-MWCNT/Ni_2B nanocatalyst were investigated for the one-pot synthesis of 3,3-dimethyl-11-phenyl-2,3,4,5,10,11-hexahydro-1*H*-dibenzo[*b*,*e*][1,4]diazepin-1-one by the reaction of *o*-phenylenediamine (**1**), and dimedone (**2**), and benzaldehyde (**3a**) as a reaction model under optimized conditions up to 4 runs (Fig. 14). After completion of the reaction model as a fresh run with 83% yield, the as-prepared Fe_3O_4/f-MWCNT/Ni_2B nanocomposite was recovered from the reaction pot using an external magnet, washed several times with deionized water and ethanol to remove any contaminants, dried at 60 °C in an oven, and used for the next run of the reaction. As depicted in Fig. 14, the nanocatalyst exhibited favorable reusability over four cycles, with no significant decline in its activity and catalytic efficiency. The yield and reaction time, altered from 83%–30 min (first run) to 72%–48 min (fourth run). This slight reduction in the reaction yield might be related to a gradual decrease in the nanocatalyst through repeated magnetic separation and washing.

To appraise the stability of the nanosystem, the leaching of Ni after 4 run recycling was determined by EDX analysis, which found a slight reduction in the amount of Ni from 6.03% to 5.89% (Fig. 15a). This suggests that the metal percentage remains relatively stable throughout the recycling process, indicating strong binding of the metal boride to the support and negligible leaching of Ni during the reaction. Also, as can be seen in the TEM images (Fig. 15b), the structure and morphology of the recycled aforementioned nanocomposite compared with the fresh one approximately remained unchanged.

3.3.4 Comparative study. In order to evince the effectiveness and high worth of the proposed procedure, a comprehensive comparison of the current protocol with various protocols reported in the literature for the one-pot synthesis of 1,4-benzodiazepines is summarized in Table 5. Key factors considered in the comparison included catalyst loading, reaction time, favorable yield, and reaction conditions. This comparative investigation elucidates that our synthetic protocol outperforms most of the reported methods due to its reduced reaction time, catalyst loading, and favorable yields of desired products.

4 Conclusion and future perspective

In conclusion, the Fe_3O_4/f-MWCNT/Ni_2B nanocomposite as a new magnetic nanocatalyst was successfully synthesized and characterized using various analytical techniques such as FT-IR,

XRD, FESEM, SEM-based EDX, SEM-based elemental mapping, HRTEM, DLS, SAED, XPS, BET, TGA, and VSM. Its unique efficacy in organic synthesis was investigated through a one-pot multi-component reaction for the synthesis of diverse 1,4-benzodiazepines, which hold chemical and potential biological significance, *via* a reaction involving *o*-phenylenediamine (**1**), dimedone (**2**), and aliphatic/aromatic/heteroaromatic aldehydes (**3a–o**). The application of this nanosystem in the aforementioned reaction resulted in the production of pure products with good-to-high yields, favorable TONs and TOFs, and acceptable reaction times. The current method proves highly suitable for obtaining a broad scope of drug-like BZD-based scaffolds, which are considered valuable heterocyclic compounds in the pharmaceutical field. Furthermore, the as-prepared nanocomposite demonstrated excellent recyclability, as it was easily recovered from the reaction mixture using an external magnet and reused for four consecutive runs. Overall, the notable characteristics of this approach encompass the utilization of the reusable catalytic system, one-pot procedure, green solvent, readily accessible starting reactants, and effortless product filtration, as well as acceptable yields of the target products. These outstanding characteristics have rendered this new approach ecologically appealing and cost effective. It is worth mentioning that our research group's future reports will explore other applications of the above-mentioned efficient as-prepared nanocomposite system, particularly in organic synthesis.

Conflicts of interest

The authors declare no conflicts of interest.

Acknowledgements

The authors gratefully acknowledge the research council of Urmia University for the financial support for this research.

References

1 N. Arora, P. Dhiman, S. Kumar, G. Singh and V. Monga, *Bioorg. Chem.*, 2020, **97**, 103668.
2 R. M. McKernan, T. W. Rosahl, D. S. Reynolds, C. Sur, K. A. Wafford, J. R. Atack, S. Farrar, J. Myers, G. Cook, P. Ferris, L. Garrett, L. Bristow, G. Marshall, A. Macaulay, N. Brown, O. Howell, K. W. Moore, R. W. Carling, L. J. Street, J. L. Castro, C. I. Ragan, G. R. Dawson and P. J. Whiting, *Nat. Neurosci.*, 2000, **3**, 587–592.
3 G. Maiti, U. Kayal, R. Karmakar and R. N. Bhattacharya, *Tetrahedron Lett.*, 2012, **53**, 1460–1463.
4 F. Crestani, K. Löw, R. Keist, M. Mandelli, H. Möhler and U. Rudolph, *Mol. Pharmacol.*, 2001, **59**, 442–445.
5 P. Salve and D. S. Mali, *Int. J. Pharma Bio Sci.*, 2013, **4**, P345–P370.
6 N. Eleftheriadis, C. G. Neochoritis, C. A. Tsoleridis, J. Stephanidou-Stephanatou and Z. Iakovidou-Kritsi, *Eur. J. Med. Chem.*, 2013, **67**, 302–309.
7 (*a*) N. Arora, P. Dhiman, S. Kumar, G. Singh and V. Monga, *Bioorg. Chem.*, 2020, **97**, 103668; (*b*) A. S. Bhathiwal, A. Bendi and A. Tiwari, *J. Mol. Struct.*, 2022, **1258**, 132649.
8 Y.-t. Ng and S. D. Collins, *Neurotherapeutics*, 2007, **4**, 138–144.
9 A. Fitton and R. C. Heel, *Drugs*, 1990, **40**, 722–747.
10 K. Löw, F. Crestani, R. Keist, D. Benke, I. Brünig, J. A. Benson, J. M. Fritschy, T. Rülicke, H. Bluethmann, H. Möhler and U. Rudolph, *Science*, 2000, **290**, 131–134.
11 (*a*) A. Almasirad, M. Ghadimi, S. Mirahmadi, P. Ahmadian Kodakan, R. Jahani, M. Nazari, E. Rezaee, H. Azizian, P. Rabizadeh, S. A. Tabatabai and M. Faizi, *Mol. Diversity*, 2022, **26**, 769–780; (*b*) H. Uchida, T. Suzuki, D. C. Mamo, B. H. Mulsant, T. Kikuchi, H. Takeuchi, M. Tomita, K. Watanabe, G. Yagi and H. Kashima, *J. Anxiety Disord.*, 2009, **23**, 477–481.
12 (*a*) N. S. Chowdari, Y. Zhang, I. McDonald, W. Johnson, D. R. Langley, P. Sivaprakasam, R. Mate, T. Huynh, S. Kotapati, M. Deshpande, C. Pan, D. Menezes, Y. Wang, C. Rao, G. Sarma, B. M. Warrack, V. S. Rangan, S. Mei-Chen, P. Cardarelli, S. Deshpande, D. Passmore, R. Rampulla, A. Mathur, R. Borzilleri, A. Rajpal, G. Vite and S. Gangwar, *J. Med. Chem.*, 2020, **63**, 13913–13950; (*b*) S. J. Gawandi, V. G. Desai, S. Joshi, S. Shingade and R. R. Pissurlenkar, *Bioorg. Chem.*, 2021, **117**, 105331.
13 X.-Q. Pan, J.-P. Zou, Z.-H. Huang and W. Zhang, *Tetrahedron Lett.*, 2008, **49**, 5302–5308.
14 L.-Z. Wang, X.-Q. Li and Y.-S. An, *Org. Biomol. Chem.*, 2015, **13**, 5497–5509.
15 A. A. Carmine and R. N. Brogden, *Drugs*, 1985, **30**, 85–126.
16 W.-B. Yi and C. Cai, *J. Fluorine Chem.*, 2009, **130**, 1054–1058.
17 D. J. Lauffer and M. D. Mullican, *Bioorg. Med. Chem. Lett.*, 2002, **12**, 1225–1227.
18 (*a*) H. Farhid, V. Khodkari, M. T. Nazeri, S. Javanbakht and A. Shaabani, *Org. Biomol. Chem.*, 2021, **19**, 3318–3358; (*b*) J. Schimer, P. Cígler, J. Veselý, K. Grantz Šašková, M. Lepšík, J. Brynda, P. Řezáčová, M. Kožíšek, I. Císařová, H. Oberwinkler, H.-G. Kraeusslich and J. Konvalinka, *J. Med. Chem.*, 2012, **55**, 10130–10135.
19 K. A. Parker and A. Dermatakis, *J. Org. Chem.*, 1997, **62**, 4164–4167.
20 N. Zohreh, A. Alizadeh, H. R. Bijanzadeh and L.-G. Zhu, *J. Comb. Chem.*, 2010, **12**, 497–502.
21 B. Pelletier, S. Duhamel, G. Tambutet, S. Jarvis, P. Cléroux, M. David, P.-L. Tanguay, L. Voisin, C. James, R. Lavoie, Y. Gareau, J. Flynn-Robitaille, T. Lorca, R. Ruel, A. Marinier and S. Meloche, *ACS Chem. Biol.*, 2023, **18**, 1039–1046.
22 S. M. Anil, R. Shobith, K. R. Kiran, T. R. Swaroop, N. Mallesha and M. P. Sadashiva, *New J. Chem.*, 2019, **43**, 182–187.
23 P. Fruscella, M. Sottocorno, M. Di Braccio, L. Diomede, N. Piccardi, A. Cagnotto, G. Grossi, M. Romano, T. Mennini and G. Roma, *Pharmacol. Res.*, 2001, **43**, 445–452.
24 M. Mehrazar, M. Hassankalhori, M. Toolabi, F. Goli, S. Moghimi, H. Nadri, S. N. A. Bukhari, L. Firoozpour and A. Foroumadi, *Mol. Diversity*, 2020, **24**, 997–1013.

25 A. Ursini, A. M. Capelli, R. A. E. Carr, P. Cassarà, M. Corsi, O. Curcuruto, G. Curotto, M. Dal Cin, S. Davalli, D. Donati, A. Feriani, H. Finch, G. Finizia, G. Gaviraghi, M. Marien, G. Pentassuglia, S. Polinelli, E. Ratti, A. Reggiani, G. Tarzia, G. Tedesco, M. E. Tranquillini, D. G. Trist and F. T. M. Van Amsterdam, *J. Med. Chem.*, 2000, **43**, 3596–3613.

26 S. Kar, H. Sanderson, K. Roy, E. Benfenati and J. Leszczynski, *Chem. Rev.*, 2022, **122**, 3637–3710.

27 (*a*) S. G. Koenig, C. Bee, A. Borovika, C. Briddell, J. Colberg, G. R. Humphrey, M. E. Kopach, I. Martinez, S. Nambiar, S. V. Plummer, S. D. Ribe, F. Roschangar, J. P. Scott and H. F. Sneddon, *ACS Sustainable Chem. Eng.*, 2019, **7**, 16937–16951; (*b*) M. Rimaz, Z. Jalalian, H. Mousavi and R. H. Prager, *Tetrahedron Lett.*, 2016, **57**, 105–109; (*c*) M. Rimaz, H. Mousavi, M. Behnam and B. Khalili, *Curr. Chem. Lett.*, 2016, **5**, 145–154; (*d*) H. Mousavi, B. Zeynizadeh, R. Younesi and M. Esmati, *Aust. J. Chem.*, 2018, **71**, 595–660; (*e*) M. Rimaz, H. Mousavi, B. Khalili and F. Aali, *J. Chin. Chem. Soc.*, 2018, **65**, 1389–1397; (*f*) B. Zeynizadeh, F. Mohammad Aminzadeh and H. Mousavi, *Res. Chem. Intermed.*, 2021, **47**, 3289–3312; (*g*) H. Galehban, B. Zeynizadeh and H. Mousavi, *J. Mol. Struct.*, 2023, **1271**, 134017; (*h*) H. C. Erythropel, J. B. Zimmerman, T. M. de Winter, L. Petitjean, F. Melnikov, C. H. Lam, A. W. Lounsbury, K. E. Mellor, N. Z. Janković, Q. Tu, L. N. Pincus, M. M. Falinski, W. Shi, P. Coish, D. L. Plata and P. A. Anastas, *Green Chem.*, 2018, **20**, 1929–1961.

28 (*a*) R. O. Rocha, M. O. Rodrigues and B. A. D. Neto, *ACS Omega*, 2020, **5**, 972–979; (*b*) H. Mousavi, *J. Mol. Struct.*, 2022, **1251**, 131742; (*c*) K. De, P. Bhanja, A. Bhaumik and C. Mukhopadhyay, *ChemCatChem*, 2018, **10**, 590–600; (*d*) S. Ray, A. Bhaumik, B. Banerjee, P. Manna and C. Mukhopadhyay, *Monatsh. Chem.*, 2015, **146**, 1881–1890; (*e*) M. Rimaz, H. Mousavi, M. Behnam, L. Sarvari and B. Khalili, *Curr. Chem. Lett.*, 2017, **6**, 55–68.

29 H. A. Younus, M. Al-Rashida, A. Hameed, M. Uroos, U. Salar, S. Rana and K. M. Khan, *Expert Opin. Ther. Pat.*, 2021, **31**, 267–289.

30 (*a*) H. Mousavi, B. Zeynizadeh and M. Rimaz, *Bioorg. Chem.*, 2023, **135**, 106390; (*b*) S. E. John, S. Gulati and N. Shankaraiah, *Org. Chem. Front.*, 2021, **8**, 4237–4287; (*c*) B. A. D. Neto, R. O. Rocha and M. O. Rodrigues, *Molecules*, 2022, **27**(1), 132; (*d*) H. Mousavi, *Int. J. Biol. Macromol.*, 2021, **186**, 1003–1166; (*e*) M. Rimaz and H. Mousavi, *Turk. J. Chem.*, 2013, **37**, 252–261; (*f*) M. Rimaz, J. Khalafy, H. Mousavi, S. Bohlooli and B. Khalili, *J. Heterocycl. Chem.*, 2017, **54**, 3174–3186; (*g*) M. Rimaz, J. Khalafy and H. Mousavi, *Res. Chem. Intermed.*, 2016, **42**, 8185–8200; (*h*) M. Rimaz, H. Mousavi, L. Ozzar and B. Khalili, *Res. Chem. Intermed.*, 2019, **45**, 2673–2694; (*i*) M. Rimaz, H. Mousavi, B. Khalili and L. Sarvari, *J. Iran. Chem. Soc.*, 2019, **16**, 1687–1701; (*j*) M. Rimaz, B. Khalili, G. Khatyal, H. Mousavi and F. Aali, *Aust. J. Chem.*, 2017, **70**, 1274–1284; (*k*) M. Rimaz, H. Mousavi, L. Nikpey and B. Khalili, *Res. Chem. Intermed.*, 2017, **43**, 3925–3937; (*l*) M. Rimaz, H. Mousavi, P. Keshavarz and B. Khalili, *Curr. Chem. Lett.*, 2015, **4**, 159–168; (*m*) B. Zeynizadeh, H. Mousavi and S. Zarrin, *J. Chin. Chem. Soc.*, 2019, **66**, 928–933; (*n*) B. Zeynizadeh, F. Mohammad Aminzadeh and H. Mousavi, *Green Process. Synth.*, 2019, **8**, 742–755; (*o*) H. Veisi, M. Pirhayati, P. Mohammadi, T. Tamoradi, S. Hemmati and B. Karmakar, *RSC Adv.*, 2023, **13**, 20530–20556.

31 (*a*) H. M. Ali, Y. A. El-Ossaily, S. A. Metwally, I. O. Althobaiti, H. A. Altaleb, Y. A. Naffea and M. S. Tolba, *ACS Omega*, 2022, **7**, 29142–29152; (*b*) B. Mirhosseini-Eshkevari, F. Zamani and M. A. Ghasemzadeh, *ChemistrySelect*, 2020, **5**, 14554–14558.

32 E. Ruijter and R. V. A. Orru, *Drug Discovery Today: Technol.*, 2013, **10**, e15–e20.

33 A. Singh, V. Palakollu, A. Pandey, S. Kanvah and S. Sharma, *RSC Adv.*, 2016, **6**, 103455–103462.

34 N. Kausar, P. Mukherjee and A. R. Das, *RSC Adv.*, 2016, **6**, 88904–88910.

35 M. Shoeb, M. Mobin, A. Ali, S. Zaman and A. H. Naqvi, *Appl. Organomet. Chem.*, 2018, **32**, e3961.

36 S. Pourghasem, F. Moeinpour and F. S. Mohseni-Shahri, *Arabian J. Chem.*, 2023, **16**, 104694.

37 X. T. Zhu, J. Y. Liu, B. Jiang and S. J. Tu, *J. Heterocycl. Chem.*, 2015, **52**, 92–96.

38 K. S. Indalkar, M. S. Patil and G. U. Chaturbhuj, *Tetrahedron Lett.*, 2017, **58**, 4496–4502.

39 Z. Karimi-Jaberi and A. Hooshmandpour, *Polycyclic Aromat. Compd.*, 2020, **40**, 432–436.

40 S. Nagaraju, O. Perumal P, K. Divakar, B. Paplal and D. Kashinath, *New J. Chem.*, 2017, **41**, 8993–9001.

41 A. Maleki, R. Firouzi-Haji and P. Farahani, *Org. Chem. Res.*, 2018, **4**, 86–94.

42 S. Tarannum and Z. N. Siddiqui, *RSC Adv.*, 2015, **5**, 74242–74250.

43 R. Mozafari and M. Ghadermazi, *RSC Adv.*, 2020, **10**, 15052–15064.

44 A. Savari, F. Heidarizadeh and N. Pourreza, *Polyhedron*, 2019, **166**, 233–247.

45 M. Esfandiari, A. Kareem Abbas, H. Shahbazi-Alavi and J. Safaei-Ghomi, *Polycyclic Aromat. Compd.*, 2022, **42**, 1235–1248.

46 S. K. Ghadiri, S. M. Baghbanian and S. Khaksar, *J. Mol. Struct.*, 2023, **1272**, 134057.

47 H. Naeimi and H. Foroughi, *Chin. J. Phys.*, 2015, **36**, 734–741.

48 H. Naeimi and H. Foroughi, *New J. Chem.*, 2015, **39**, 1228–1236.

49 A. Maleki and M. Kamalzare, *Tetrahedron Lett.*, 2014, **55**, 6931–6934.

50 M. Moeini korbekandi, M. Nasr-Esfahani, I. Mohammadpoor-Baltork, M. Moghadam, S. Tangestaninejad and V. Mirkhani, *Catal. Lett.*, 2019, **149**, 1057–1066.

51 T. Ahmadi, G. Mohammadi Ziarani, S. M. Masoumian Hoseini, A. Badiei and M. M. Ranjbar, *J. Iran. Chem. Soc.*, 2021, **18**, 2047–2056.

52 M. Esfandiari, A. K. Abbas, M. R. Vakili, H. Shahbazi-Alavi and J. Safaei-Ghomi, *Res. Chem. Intermed.*, 2021, **47**, 483–496.

53 K. Bhagat, A. Singh, S. Dhiman, J. Vir Singh, R. Kaur, G. Kaur, H. Kaur Gulati, P. Singh, R. Kumar, R. Salwan, K. Bhagat,

H. Singh, S. Sharma and P. M. Singh Bedi, *Med. Chem. Res.*, 2019, **28**, 2200–2217.
54 Y. Wang, M.-S. Tu, F. Shi and S.-J. Tu, *Adv. Synth. Catal.*, 2014, **356**, 2009–2019.
55 J. N. Sangshetti, R. S. Chouthe, M. R. Jadhav, N. S. Sakle, A. Chabukswar, I. Gonjari, S. Darandale and D. B. Shinde, *Arabian J. Chem.*, 2017, **10**, S1356–S1363.
56 S. Iijima, *Nature*, 1991, **354**, 56–58.
57 A. Stegarescu, H. Cabrera, H. Budasheva, M. L. Soran, I. Lung, F. Limosani, D. Korte, M. Amati, G. Borodi, I. Kacso, O. Opriș, M. Dan and S. Bellucci, *Nanomaterials*, 2022, **12**(17), 3008.
58 (*a*) H. Abbasi, M. Antunes and J. I. Velasco, *Prog. Mater. Sci.*, 2019, **103**, 319–373; (*b*) R. Zou, F. Liu, N. Hu, H. Ning, Y. Gong, S. Wang, K. Huang, X. Jiang, C. Xu, S. Fu, Y. Li and C. Yan, *ACS Appl. Mater. Interfaces*, 2020, **12**, 57391–57400; (*c*) H. Wang, X. Sun, Y. Wang, K. Li, J. Wang, X. Dai, B. Chen, D. Chong, L. Zhang and J. Yan, *Nat. Commun.*, 2023, **14**, 380.
59 J. L. Blackburn, A. J. Ferguson, C. Cho and J. C. Grunlan, *Adv. Mater.*, 2018, **30**, 1704386.
60 (*a*) D. Tasis, N. Tagmatarchis, A. Bianco and M. Prato, *Chem. Rev.*, 2006, **106**, 1105–1136; (*b*) A. Hirsch, *Angew. Chem., Int. Ed.*, 2002, **41**, 1853–1859.
61 Y. P. Sun, K. Fu, Y. Lin and W. Huang, *Acc. Chem. Res.*, 2002, **35**, 1096–1104.
62 O. K. Kim, J. Je, J. W. Baldwin, S. Kooi, P. E. Pehrsson and L. J. Buckley, *J. Am. Chem. Soc.*, 2003, **125**, 4426–4427.
63 M. A. Kabbani, C. S. Tiwary, P. A. S. Autreto, G. Brunetto, A. Som, K. R. Krishnadas, S. Ozden, K. P. Hackenberg, Y. Gong, D. S. Galvao, R. Vajtai, A. T. Kabbani, T. Pradeep and P. M. Ajayan, *Nat. Commun.*, 2015, **6**, 7291.
64 X. Gu, W. Qi, S. Wu, Z. Sun, X. Xu and D. Su, *Catal. Sci. Technol.*, 2014, **4**, 1730–1733.
65 H. Ajiki and T. Ando, *J. Phys. Soc. Jpn.*, 1994, **63**, 4267.
66 J. Tuček, K. C. Kemp, K. S. Kim and R. Zbořil, *ACS Nano*, 2014, **8**, 7571–7612.
67 (*a*) N. Panwar, A. M. Soehartono, K. K. Chan, S. Zeng, G. Xu, J. Qu, P. Coquet, K.-T. Yong and X. Chen, *Chem. Rev.*, 2019, **119**, 9559–9656; (*b*) M. Samadishadlou, M. Farshbaf, N. Annabi, T. Kavetskyy, R. Khalilov, S. Saghfi, A. Akbarzadeh and S. Mousavi, *Artif. Cells, Nanomed., Biotechnol.*, 2018, **46**, 1314–1330; (*c*) S. Boncel, A. P. Herman and K. Z. Walczak, *J. Mater. Chem.*, 2012, **22**, 31–37; (*d*) A. S. Andreev, M. A. Kazakova, A. V. Ishchenko, A. G. Selyutin, O. B. Lapina, V. L. Kuznetsov and J.-B. d'Espinose de Lacaillerie, *Carbon*, 2017, **114**, 39–49; (*e*) J. Tuček, K. C. Kemp, K. S. Kim and R. Zbořil, *ACS Nano*, 2014, **8**, 7571–7612; (*f*) J. N. Tiwari, V. Vij, K. C. Kemp and K. S. Kim, *ACS Nano*, 2016, **10**, 46–80.
68 (*a*) Y. Huaccallo-Aguilar, S. Álvarez-Torrellas, M. Larriba, V. I. Águeda, J. A. Delgado, G. Ovejero and J. García, *Catalysts*, 2019, **9**, 287; (*b*) S. K. Folsom, D. J. Ivey, F. S. McNair and A. R. Siamaki, *Catalysts*, 2021, **11**, 495.
69 (*a*) M. Ghereghlou, A. A. Esmaeili and M. Darroudi, *Appl. Organomet. Chem.*, 2021, **35**, e6387; (*b*) S. Karami and B. Zeynizadeh, *Green Process. Synth.*, 2019, **211**, 298–307.
70 Y. Kang, Y. Tang, L. Zhu, B. Jiang, X. Xu, O. Guselnikova, H. Li, T. Asahi and Y. Yamauchi, *ACS Catal.*, 2022, **12**, 14773–14793.
71 (*a*) B. Zeynizadeh, R. Younesi and H. Mousavi, *Res. Chem. Intermed.*, 2018, **44**, 7331–7352; (*b*) Y. Cheng, M. Tanaka, T. Watanabe, S. Y. Choi, M. S. Shin and K. H. Lee, *J. Phys.: Conf. Ser.*, 2014, **518**, 012026; (*c*) A. A. Madjdabadi, R. Beugelmans and A. Lechevallier, *Synth. Commun.*, 1989, **19**, 1631–1640; (*d*) R. Tian, S. Zhao, J. Li, Z. Chen, W. Peng, Y. He, L. Zhang, S. Yan, L. Wu, R. Ahuja and H. Gou, *J. Mater. Chem. A*, 2021, **9**, 6469–6475; (*e*) C. A. Brown, *J. Chem. Soc. D*, 1969, 952, DOI: **10.1039/C29690000952**; (*f*) R. Sarkar, S. K. Samanta, A. Hasija, D. Chopra, D. Ganguly and M. K. Bera, *New J. Chem.*, 2022, **46**, 7168–7176; (*g*) X. Chen, Z. Yu, L. Wei, Z. Zhou, S. Zhai, J. Chen, Y. Wang, Q. Huang, H. E. Karahan, X. Liao and Y. Chen, *J. Mater. Chem. A*, 2019, **7**, 764–774; (*h*) Y. Qi, Y. Zhang, L. Yang, Y. Zhao, Y. Zhu, H. Jiang and C. Li, *Nat. Commun.*, 2022, **13**, 4602; (*i*) J. Masa, I. Sinev, H. Mistry, E. Ventosa, M. de la Mata, J. Arbiol, M. Muhler, B. Roldan Cuenya and W. Schuhmann, *Adv. Energy Mater.*, 2017, **7**, 1700381; (*j*) F. Taghavi, C. Falamaki, A. Shabanov, L. Bayrami and A. Roumianfar, *Appl. Catal., A*, 2011, **407**, 173–180; (*k*) F. Taghavi, C. Falamaki, A. Shabanov, M. Seyyedi and M. Zare, *Appl. Catal., A*, 2013, **453**, 334–340.
72 M. Shahbazi, H. Cathey, N. Danilova and I. D. R. Mackinnon, *Materials*, 2018, **11**(7), 1259.
73 (*a*) A. Z. O. Ali, A. Masoudi and R. Soliyman, *J. Nanomed. Nanotechnol.*, 2017, **8**, 1000477; (*b*) F. Escalettes, D. Florentin, A. Marquet, C. Canlet and J. Courtieu, *Tetrahedron Lett.*, 1998, **39**, 7499–7502.
74 (*a*) H. Türkez, M. E. Arslan, E. Sönmez, A. Tatar, F. Geyikoğlu, M. Açikyildiz and A. Mardinoğlu, *Biol. Trace Elem. Res.*, 2021, **199**, 2602–2611; (*b*) C. T. Zhou, J. D. Xing, B. Xiao, J. Feng, X. J. Xie and Y. H. Chen, *Comput. Mater. Sci.*, 2009, **44**, 1056–1064; (*c*) M. Wang, J. Xie, K. Xue and L. Li, *Comput. Mater. Sci.*, 2021, **194**, 110465.
75 H. Türkez, M. E. Arslan, E. Sönmez, A. Tatar, F. Geyikoğlu, M. Açikyildiz and A. Mardinoğlu, *Biol. Trace Elem. Res.*, 2021, **199**, 2602–2611.
76 (*a*) B. Zeynizadeh and S. Rahmani, *RSC Adv.*, 2019, **9**, 28038–28052; (*b*) B. Zeynizadeh and S. Rahmani, *RSC Adv.*, 2019, **9**, 8002–8015; (*c*) M. Hasanpour Galehban, B. Zeynizadeh and H. Mousavi, *RSC Adv.*, 2022, **12**, 11164–11189; (*d*) B. Zeynizadeh, F. Mohammad Aminzadeh and H. Mousavi, *Res. Chem. Intermed.*, 2019, **45**, 3329–3357.
77 (*a*) H. Mousavi, B. Zeynizadeh and M. Rimaz, *Bioorg. Chem.*, 2023, **135**, 106390; (*b*) H. Galehban, B. Zeynizadeh and H. Mousavi, *RSC Adv.*, 2022, **12**, 16454–16478; (*c*) M. Bayzidi and B. Zeynizadeh, *ChemistrySelect*, 2022, **7**, e202202708.
78 M. H. Ramezan zadeh, M. Seifi, H. Hekmatara and M. B. Askari, *Chin. J. Phys.*, 2017, **55**, 1319–1328.
79 F. Taghavi, C. Falamaki, A. Shabanov, L. Bairami and M. Seyyedi, *React. Kinet., Mech. Catal.*, 2013, **109**, 91–104.
80 J. Legrand, S. Gota, M. J. Guittet and C. Petit, *Langmuir*, 2002, **18**, 4131–4137.

81 M. Moazzen, A. Mousavi Khaneghah, N. Shariatifar, M. Ahmadloo, I. Eş, A. N. Baghani, S. Yousefinejad, M. Alimohammadi, A. Azari, S. Dobaradaran, N. Rastkari, S. Nazmara, M. Delikhoon and G. Jahed Khaniki, *Arabian J. Chem.*, 2019, **12**, 476–488.

82 (*a*) V. Soum, S. Park, A. I. Brilian, Y. Kim, M. Y. Ryu, T. Brazell, F. J. Burpo, K. K. Parker, O.-S. Kwon and K. Shin, *ACS Omega*, 2019, **4**, 8626–8631; (*b*) K. Dai, G. Dawson, S. Yang, Z. Chen and L. Lu, *Chem. Eng. J.*, 2012, **191**, 571–578; (*c*) W. Zhang, V. Stolojan, S. R. P. Silva and C. W. Wu, *Spectrochim. Acta, Part A*, 2014, **121**, 715–718.

83 (*a*) K. Zhao, T. Xu, J. Cao, L. Yang, M. Wei, H. Fan, H. Liu, C. Liu and X. Liu, *J. Mater. Sci.: Mater. Electron.*, 2019, **30**, 18802–18810; (*b*) J. Masa, I. Sinev, H. Mistry, E. Ventosa, M. de la Mata, J. Arbiol, M. Muhler, B. Roldan Cuenya and W. Schuhmann, *Adv. Energy Mater.*, 2017, **7**, 1700381.

84 (*a*) T. I. T. Okpalugo, P. Papakonstantinou, H. Murphy, J. McLaughlin and N. M. D. Brown, *Carbon*, 2005, **43**, 153–161; (*b*) S. Li, Z. Li, B. Ke, Z. He, Y. Cui, Z. Pan, D. Li, S. Huang, C. Lai and J. Su, *J. Mol. Liq.*, 2019, **279**, 241–250; (*c*) V. B. Koli, A. G. Dhodamani, A. V. Raut, N. D. Thorat, S. H. Pawar and S. D. Delekar, *J. Photochem. Photobiol., A*, 2016, **328**, 50–58.

85 Q. Tang, B. Li, W. Ma, H. Gao, H. Zhou, C. Yang, Y. Gao and D. Wang, *Environ. Sci. Pollut. Res.*, 2020, **27**, 18773–18783.

86 (*a*) W. Zhao, C. Liang, B. Wang and S. Xing, *ACS Appl. Mater. Interfaces*, 2017, **9**, 41927–41936; (*b*) G. Tong, Y. Liu, T. Wu, Y. Ye and C. Tong, *Nanoscale*, 2015, **7**, 16493–16503.

87 (*a*) A. P. Grosvenor, B. A. Kobe, M. C. Biesinger and N. S. McIntyre, *Surf. Interface Anal.*, 2004, **36**, 1564–1574; (*b*) Q. Ai, Z. Yuan, R. Huang, C. Yang, G. Jiang, J. Xiong, Z. Huang and S. Yuan, *J. Mater. Sci.*, 2019, **54**, 4212–4224.

88 X. Cao, X. Wang, L. Cui, D. Jiang, Y. Zheng and J. Liu, *Chem. Eng. J.*, 2017, **327**, 1085–1092.

89 C. Wu, Y. Bai, D.-X. Liu, F. Wu, M.-L. Pang and B.-L. Yi, *Catal. Today*, 2011, **170**, 33–39.

90 J. Masa, P. Weide, D. Peeters, I. Sinev, W. Xia, Z. Sun, C. Somsen, M. Muhler and W. Schuhmann, *Adv. Energy Mater.*, 2016, **6**, 1502313.

91 (*a*) X. Jia, B. Liu, J. Liu, S. Zhang, Z. Sun, X. He, H. Li, G. Wang and H. Chang, *RSC Adv.*, 2021, **11**, 10753–10759; (*b*) L. Li, Z. Deng, L. Yu, Z. Lin, W. Wang and G. Yang, *Nano Energy*, 2016, **27**, 103–113.

92 B. J. Matsoso, K. Ranganathan, B. K. Mutuma, T. Lerotholi, G. Jones and N. J. Coville, *New J. Chem.*, 2017, **41**, 9497–9504.

93 S. Brunauer, P. H. Emmett and E. Teller, *J. Am. Chem. Soc.*, 1938, **60**, 309–319.

94 (*a*) M. Aghababaei, A. A. Ghoreyshi and K. Esfandiari, *Int. J. Hydrogen Energy*, 2020, **45**, 23112–23121; (*b*) L. Wan, D. Yan, X. Xu, J. Li, T. Lu, Y. Gao, Y. Yao and L. Pan, *J. Mater. Chem. A*, 2018, **6**, 24940–24948; (*c*) G. Yuan, J. Pan, Y. Zhang, J. Yu, Y. He, Y. Su, Q. Zhou, H. Jin and S. Xie, *RSC Adv.*, 2018, **8**, 17950–17957; (*d*) A. H. Norzilah, A. Fakhru'l-Razi, T. S. Y. Choong and A. L. Chuah, *J. Nanomater.*, 2011, 495676; (*e*) E. Zong, X. Liu, J. Wang, S. Yang, J. Jiang and S. Fu, *J. Mater. Sci.*, 2017, **52**, 7294–7310.

95 Y.-J. Han and S.-J. Park, *Appl. Surf. Sci.*, 2017, **415**, 85–89.

96 (*a*) M. Aghababaei, A. A. Ghoreyshi and K. Esfandiari, *Introd. Hydrogen Energy*, 2020, **45**, 23112–23121; (*b*) J. Ye, S. Wu, K. Ni, Z. Tan, J. Xu, Z. Tao and Y. Zhu, *Chemphyschem*, 2017, **18**, 1929–1936; (*c*) C.-H. Chen and C.-C. Huang, *Sep. Purif. Technol.*, 2009, **65**, 305–310.

97 Y. H. Tan, J. A. Davis, K. Fujikawa, N. V. Ganesh, A. V. Demchenko and K. J. Stine, *J. Mater. Chem.*, 2012, **22**, 6733–6745.

98 B. Zeynizadeh, H. Mousavi and F. Sepehraddin, *Res. Chem. Intermed.*, 2020, **46**, 3361–3382.

99 T. T. Wen and L. Z. Wang, *Mater. Today Chem.*, 2022, **26**, 101071.